DAMPING CHARACTERISTICS OF WAVE PROPAGATION ACROSS THE MUDDY LOUISIANA SHELF

A thesis submitted to the faculty of
San Francisco State University
In partial fulfillment for
The degree

Master of Science
In
Geosciences

by

Anita Cathrine Engelstad

San Francisco, California

May, 2011

CERTIFICATION OF APPROVAL

I certify that I have read *Damping characteristics of wave propagation across the muddy Louisiana shelf* by Anita Cathrine Engelstad, and that in my opinion this works meets the criteria for approving a thesis submitted in partial fulfillment of the requirements for the degree: Master of Science in Geosciences: Physical Oceanography at San Francisco State University.

Dr. Tim Janssen
Assistant Professor of Oceanography

Dr. Newell (Toby) Garfield
Professor of Oceanography

Dr. Thomas H.C. Herbers
Professor of Oceanography,
Naval Postgraduate School, Monterey

DAMPING CHARACTERISTICS OF WAVE PROPAGATION ACROSS THE MUDDY LOUISIANA SHELF

Anita Cathrine Engelstad
San Francisco, California
2011

To improve the understanding of the effect of a muddy seafloor on wave dynamics, a new data set, collected on the muddy Louisiana coast in the spring of 2008, is analyzed. Waves were observed for two months at 32 locations along a 25 km transect between 13- and 2-m water depth. To investigate the effects of mud on the nearshore wave energy balance, the SWAN wave model was used to hindcast the observational period, using a standard JONSWAP bottom friction term for wave-bottom interaction to represent wave propagation across a sandy shelf. The findings show that the interaction between mud and waves is episodic. We identify two types of wave-mud damping events, where either 1) the damping occurs in the energetic ranges of the spectrum, generally stronger at lower frequencies, or 2) wave growth is suppressed during times of heightened sediment concentrations throughout the water column. Our observations suggest that currents play an important role in the resuspension of sediments.

I certify that the Abstract is a correct representation of the content of this thesis.

Chair, Thesis Committee

Date May 12, 2011

ACKNOWLEDGEMENTS

First, I want to thank Tim Janssen. His support and encouragement throughout this project went beyond anything I could have hoped for. He generously shared his resources, his profound knowledge, and much of his time. I would like to thank Toby Garfield and Tom Herbers for their valuable comments and suggestions.

I am grateful that I was able to use the data collected by the teams from the Naval Postgraduate School, Scripps Institution of Oceanography, and Woods Hole Oceanographic Institution. Many thanks to Steve Elgar and Britt Raubenheimer, who prepared and shared their data, and who were wonderful editors for our two posters. I would also like to thank Gerbrant van Vledder who suggested the scaling method for the wind field and provided me with code, information about the SWAN model, and helpful discussions. The support from The Office of Naval Research (ONR) was much appreciated.

Many thanks go to the Geosciences Department for all the knowledge I gained while there and the support that I received throughout my stay. Thanks to Isaac and Sang who shared the daily ups and downs of physical oceanography with me. Most of all, I want to thank Ralf Krug, my partner in life, who inspired me and supported me throughout my school years in every imaginable way. I could not have done it without him.

TABLE OF CONTENTS

LIST OF TABLES

LIST OF FIGURES

Figure		Page

1. Introduction

To fishermen and other seafarers, it has been long known that wind-generated ocean waves are very effectively damped when crossing a muddy seafloor [Gade, 1958; Elgar & Raubenheimer, 2008]. Some examples include, the southwest coast of India where the arrival of mud-banks is celebrated since the calming effect on the ocean allows local fishermen to go out and collect the yearly fish harvest [Elgar & Raubenheimer, 2008], and the Louisiana shelf, the 'Mud-Hole' (92° 30'W), which has long been used by local fishermen as a shelter in high seas [Gade, 1958]. Although these remarkable interactions between surface waves and a muddy seafloor have received some attention [e.g. Gade, 1958; Dalrymple and Liu, 1978; Ng, 2000; Elgar and Raubenheimer, 2008], the physical mechanisms and the characteristics are still poorly understood.

Wave damping by mud has important implications for the nearshore environment. The loss of energy (and momentum) from the waves through the interaction with the mud affects coastal circulation, cross-shelf mixing, and exchange processes near the coast. In extreme cases, the energy loss across the shelf can be so dramatic that waves are too small to break by the time they reach the shore. To model and predict wave evolution and transport dynamics across a muddy shelf, and to make a step toward understanding the implications to coastal circulation, it is critical to understand the principal mechanism by which the wave energy is lost in the interaction.

Gade (1958) was the first to propose a two-layer model in which the increased damping is due to an energy transfer from the surface waves to internal waves on the density interface between the upper (usually represented as inviscid) fluid layer and a thin, highly-viscous fluid-mud layer. Gade considered waves in relatively shallow water (depth small relative to wavelength), which was later extended to include viscosity in the upper layer and arbitrary depths [e.g. Dalrymple and Liu, 1978; Ng, 2000]. Exploiting the fact that mud layers are usually relatively thin when compared to the water depth, Ng (2000) proposed a boundary-layer approximation, which results in an explicit expression for the wave-damping coefficient (the imaginary part of the wavenumber).

Wave damping is not necessarily stronger over thicker fluid-mud layers. In fact, all of the theoretical works based on the two-layer approach discussed here, show wave-mud damping to be maximum when the mud-layer is about 1.1–1.5 times the thickness of the Stokes boundary layer β, the latter being defined as [e.g. Svendsen, 2006]

$$\beta = \sqrt{\frac{\omega}{2\nu}} \quad . \qquad (1)$$

Here ω is the angular frequency of the waves, and ν is the fluid viscosity. Regardless of the mud properties, these two-layer models only predict wave damping if the water is shallow enough for the waves to actually feel the bottom (and thus the mud). However, field observations indicate that short waves, which are too short to directly interact with the seafloor, are also losing energy [e.g. Sheremet and Stone, 2003; Elgar and Raubenheimer, 2008].

Sheremet et al. (2005) proposed that resettling of suspended sediment after storms forms a high-density mud-layer in which the energy is dissipated. They suggested further that the dissipation of short waves is sustained by nonlinear three-wave (triad) interactions in which high-frequency waves are believed to transfer energy to low-frequency waves, where it is subsequently dissipated.

Further evidence of the interaction of a muddy seafloor with short wavelength surface waves was presented by Trainor (2009) who found what appeared to be a strong suppression of high-frequency energy in shallow water during fetch-limited conditions, when comparing observations of wave evolution over mud with predictions from a conventional wave model (SWAN).

The dissipation, or lack of generation, of high-frequency waves under wind-forced conditions suggests that a discrete two-layer model, which would affect mostly longer waves, may not represent the complete physics of the interaction. It remains unclear how such short waves, not directly interacting with the bottom, lose their energy [see e.g. Sheremet & Stone, 2003; Sheremet et al., 2005], or how the presence of mud on the seafloor could affect the efficiency of momentum transfer across the atmospheric boundary layer into the water.

The objective of this study is to contribute to answering these questions through a detailed analysis of a newly collected dataset of wave propagation across the muddy Louisiana shelf. The combined data set includes a wide range of wave and wind conditions, measured at 32 locations between 13- and 2-m water depths. Through detailed analysis of observed dissipation and generation rates, comparison to a third-generation wind-wave model, and the correlation of turbidity levels with the wind velocities, we will study and discuss the characteristics of wave damping as waves travel across a muddy shelf.

This work is organized as follows. In Capter 2 we introduce the study area, the instrumentation, and the data analysis. Chapter 3 describes the model and the model settings chosen for this study. The analysis of wave heights, energy flux gradients, and spectral evolution will be presented and discussed in Chapter 4. In Chapter 5 we investigate the influence of currents on the re-suspension of sediments and the subsequent correlation to wave damping. We discuss our principal findings in Chapter 6, followed by conclusions in Chapter 7.

2. Field Observations

The study area on the Louisiana shelf is located on the Chenier Plain, west of the Atchafalaya outflow (figure 1). The Atchafalaya River is one of the main tributaries of the Mississippi River and carries about 84 million metric tons of suspended sediment per year [Allison et al. et al., 2000]. Fine-grained sediment [e.g. Wells and Kemp, 1981; Allison et al., 2000; Draut et al., 2005] is carried to the west in what Wells and Kemp (1981) named the Atchafalaya mud stream. About 7±2% of the total sediment load transported by the Atchafalaya River is deposited on the eastern Chenier plain and the coastal zone, extending to ~ 92.55 ° W [Draut et al., 2005]. Deposition on the fairly flat (bottom slope O(1:1000)) shelf is restricted to approximately shoreward of the 10m isobath [Allison et al., 2000].

The local weather is influenced by coastal fronts which pass through the area on a timescale of 3-7 days, resulting in onshore, south-easterly winds before the frontal passage and offshore northerly winds after the front has passed [Allison et al., 2000]. During these cold fronts, as well as during hurricanes and tropical storms, resuspension of mud is common [Allison et al., 2000; Draut et al., 2005].

From early February 2008 through March 2008, field observations of wave propagation across the muddy shelf were acquired in the area (see figure 1). These observations were part of the Louisiana Mud Experiment (MUDEX08), conducted by research teams funded by an Office of Naval Research Multidisciplinary University Research Initiative (MURI). In this study we consider the inner shelf stations deployed by the Naval Postgraduate School (NPS) and Scripps Institution of Oceanography (SIO) teams, and the nearshore stations deployed by the Woods Hole Oceanographic Institution (WHOI) team (Elgar/Raubenheimer).

Observations on the inner shelf

The shelf stations were arranged in two cross-shore arrays and one alongshore array (see figure 2 and table 1 for locations and depths), and were deployed in water depths ranging from 13 m to 4 m (see also Trainor, 2009 for further detail).

The shelf dataset consists of observations from two Datawell Directional Waverider buoys sampling continuously at 1.28 Hz, six bottom-mounted Nortek Vector pressure-velocity instruments sampling 69-minute bursts at 2 Hz every four hours, and eight bottom-mounted pressure recorders sampling continuously at 2 Hz (see figure 2). In addition, six bottom-mounted Nortek Aquadopp Acoustic Doppler Current Profilers (ADCP) were deployed as back-up instruments for the Nortek Vectors and sampled 34-minute bursts at 1 Hz every hour.

The bottom-mounted instruments were recovered and redeployed (instrument turn-around) between March 2nd and March 5th to check instrument operation, replace batteries and retrieve the internally recorded data from the instruments. Two sensors (pa5 and pa11, see figure 2) could not be recovered during the turn-around operations, while another pressure recorder (pa10) could not be recovered at the end of the experiment. The latter sensor was also displaced by a fishing vessel during the first leg and is therefore not included in this analysis. Data from the western buoy (dw1) became intermittent during the second leg and data recorded by this instrument after March 5th 2008, are not used in this study. During the first leg, noise levels in the data from the pressure-velocity instrument at station pv4 were considered too high; these observations were discarded and observations recorded by the collocated ADCP were used instead. A meteorological buoy, operated by a WHOI team led by Dr. John Trowbridge, recorded wind speed and direction in 5-minute intervals at 3 m above sea level, and was positioned on the western transect (see figure 2), between sensors pa5 and pa6.

Box core samples to determine the rheology of the mud at each site were taken by Dr. Anna Garcia-Garcia from UC Santa Cruz [Trainor, 2009; Garcia-Garcia et al, 2011, and references therein].

Observations in the nearshore

The nearshore instrument array, deployed by the Woods Hole Oceanographic Institution (WHOI), consisted of 16 collocated pressure gauges and acoustic Doppler velocimeters (see figure 2), arranged in a cross-shore array in water depths ranging from 5 m to 2 m. The instruments were deployed between February 14th and April 17th during which time the instruments collected 51-minute bursts at 2 Hz every two hours. In this array, the position of the most onshore sensor (n01) changed over the duration of the experiment (Elgar 2009, personal communication), and the data from this instrument is discarded in our analysis. Another sensor (n10) was lost during the experiment (no data available).

The nearshore array smoothly connects to the western shelf transect (figure 2) and the combined dataset thus effectively includes an instrumented cross-shore transect of observations from 13 m water depth to the very nearshore (2 m water depth), covering a distance of about 13 km cross-shore (figure 2).

Data analysis

For the analysis presented here, we exclusively use observations from instruments on the western and the central transects recorded in the period between February 16th and March 27th, during which most sensors were operational. Where possible, instrument data were processed in hourly blocks (see table 2) to ensure compatibility between spectral estimates (and to match the sampling interval of the NPS/SIO Vector pressure-velocity sensors). Spectral analysis was performed using standard Fast Fourier Transform techniques while applying a Hamming window with 50% overlapping blocks. For all sensors, hourly spectral estimates have 256 degrees of freedom (DOF), with the exception of the spectra from ADCP observations, which - due to the shorter length of the recorded time series - have 128 degrees of freedom.

3. Model description

Model hindcasts are made using the third-generation wind-wave model SWAN (version 40.72). This class of models is based on the wave action balance (or radiative transfer equation), which – in Cartesian coordinates – can be written as [see e.g. Booij et al., 1999]

$$\frac{\partial}{\partial t}N + \nabla_{\mathbf{x}} \cdot \left(\left[\mathbf{u} + \mathbf{c}_{\mathbf{x}} \right] N \right) + \frac{\partial}{\partial \sigma} c_\sigma N + \frac{\partial}{\partial \theta} c_\theta N = \frac{S}{\sigma} \quad . \qquad (2)$$

Here $N = N(\sigma,\theta)$ is the action density defined as energy density over (relative) frequency; $\mathbf{x} = (x,y)$ are the coordinates of the physical space, and (σ,θ) are the (relative) frequency and direction coordinates of the spectral space. The $\mathbf{c}_{\mathbf{x}}$, c_σ, and c_θ represent the propagation speed of the action density in the spatial domain, in frequency space, and in directional space respectively. On the right of equation (1) $S = S(\sigma,\theta)$, usually referred to as a source term, represents the combined effects of generation (wind), dissipation (bottom friction, white capping, depth-induced wave breaking), and non-linear wave-wave interactions.

Grids and Physics

Simulations were made on a 2D computational grid, covering an area of ~ 59 x 34 km (figure 3, also see table 3 for further information). The model was run in non-stationary mode, with hourly updated wave, wind and water level variations. Wave boundary conditions for the southern boundary (see figure 3) are taken jointly from the most offshore buoy (dw12) and the easternmost pressure-velocity sensor (pv16). Side-boundaries for the domain are updated using 1D non-stationary runs (along the boundary) to prevent the occurrence of spurious shadow zones and/or energy leakage.

The model was run in third-generation mode (GEN 3), with saturation-based whitecapping [Van der Westhuysen et al., 2007] combined with the Yan wind input term [Yan, 1987]. All available source terms are included in the computations except the triad interactions.

Bottom friction

One of the objectives of the hindcast study is to identify the differences observed in the wave evolution over a muddy seafloor, relative to that anticipated over a sandy shelf. Therefore, we do not include a specific mud model [see e.g. Dalrymple & Liu, 1978; Winterwerp et al., 2007; Rogers & Holland, 2009], but instead we use a standard bottom friction term [Hasselmann et al., 1973] to account for frictional losses of wave energy that would be present over a sandy shelf.

Even though our data set consists of low-frequency swell, wind-sea, and mixed events, the JONSWAP (Joint North Sea Wave Observation Project) bottom friction coefficient is set to 0.038 m^2s^{-3}, as originally suggested by Hasselmann et al. (1973) during the JONSWAP experiment. Although a higher value for the coefficient (0.068 m^2s^{-3}) was later determined [Bouws and Komen, 1983] which was generally considered to be a better value for fully developed wind-sea conditions, Van Vledder et al. (2011), motivated by the lack of accurate SWAN - hindcasts of low-frequency energy in shallow water, showed that this result may have been inconsistent. From a detailed reanalysis of the storm observations used by Bouws and Komen, and the inclusion of two other case studies, these authors find 0.038 m^2s^{-3} to be an optimal value for the representation of bottom friction under both swell and wind-sea events. In general, we anticipate that reasonable values for this coefficient depend on particular bottom characteristics and may be expected to vary regionally. However, since the purpose here is to study the effects of a muddy shelf on coastal wave evolution relative to that over a sandy bottom, a single representative value of 0.038 m^2s^{-3} for the bottom friction coefficient appears to be the most appropriate.

Wind, bottom, and tides

Wind forcing for the model is obtained from hourly averaged meteorological observations made on the western transect (see figure 2 for location), and is corrected for winds at 10 m using the 1/7 power expression [Johnson, 1999, and references therein]

$$\frac{U_{10}}{U_z} = \left(\frac{10}{z}\right)^{\frac{1}{7}} \tag{3}$$

with U_{10} being the wind speed at 10 m and z the reference height. Comparisons to other nearby meteorological stations (LSU, NDBC-CAPL1, see figure 4 for positions) suggest that the wind in the area is fairly homogenous (figure 5). To account for the down-wind variability of the atmospheric boundary layer due to the decrease in roughness length over water, wind speeds during offshore wind events (defined as wind events with mean wind directions $< \pm\frac{\pi}{2}$ from exactly offshore) are modified by a spatially varying scaling factor [e.g.

Taylor & Lee, 1984]. A comparison of the effect of scaling the wind speed with wind speeds at the onshore NDBC buoy and offshore atmospheric model output (European Centre for Medium-Range Weather Forecasts - ECMWF) is shown in figure 6. Overall, the downscaling toward shore shows an improvement, while the effect of up-scaling seaward is difficult to evaluate since the modeled speeds are overall lower than the observations (figure 6).

Bathymetry and water level

Bathymetry information was taken from the NOS coastal relief model, augmented with nearshore observations by the WHOI team during the experiment (Elgar, personal communication). Water level variations, mostly due to tidal changes (maximum amplitude ~ 60 cm), were obtained from the observations by taking the mean (over all sensors) of the difference between the hourly-averaged, observed water depths, and the local bathymetry.

4. Analysis of wave growth and damping across the muddy shelf

To study the effects of a muddy seafloor on the evolution of wind waves we compare observations to SWAN model results run with a standard bottom friction term [Hasselmann et al., 1973]. Model results are assumed to be representative of a wave field driven by the same forcing as the observations, but without being subjected to the interaction with mud. Therefore, differences between model and observations provide an estimate of the influence of the mud on the wavefield.

To identify systematic differences between model predictions and observations we analyze time-series of wave height. To further identify the nature of the damping events, and consider the differences in generation and dissipation, we consider a simplified energy balance and the time variability of flux gradients. Special attention is paid to the spectral range where mud-damping is found, since the two-layer model requires the interaction of waves with the fluid-mud interface, which would lead primarily to the dissipation of longer wavelengths.

A first comparison of wave heights

Differences in observed wave heights relative to model estimates of waves propagating across a muddy seafloor are investigated using scatter plots for all available stations in addition to time-series comparisons for pv2 on the western transect, pv7 on the central transect, (both stations are on the same isobath in about 11 m water depth), and the nearshore sensors n16 and n04 (in ~4 m and ~1.7 m water depth, respectively).

Significant wave heights are estimated by

$$H_s = 4\sqrt{\int_{0.04}^{0.25} S(f)df} \qquad (4)$$

where the variance density (S) is integrated between 0.04 Hz and 0.25 Hz. The latter value is chosen to avoid errors due to the attenuation of the pressure signal at deeper stations and, for consistency, these limits are maintained for all stations.

The overall agreement between modeled and observed wave heights at all stations is good (figure 8) although modeled wave heights are rather somewhat overestimated. However, time-series (figure 9) reveal episodic disagreements between observations and model. To characterize the sea-state during these episodes we divide the spectrum in a low-frequency, long wave, range from 0.04 – 0.20 Hz, and a high-frequency, short-wave, range from 0.20 – 0.25 Hz[1] (Sheremet & Stone, 2003). We distinguish two types of events, which can be identified from the time-series and examine them separately. These are defined as follows.

---

[1] Note that for the short-wave range, kh values are still O(1) at the deeper stations, and therefore these "short" waves will probably still (weakly) interact with the seafloor.

Propagation-Damping (PD) events

PD events are characterized by stronger attenuation of observed wave heights compared to modeled wave heights as waves travel from offshore into the nearshore (figure 9, examples are marked by crosses). In other words, the overall decrease in wave height is greater for the observations than for the model. PD events are dominated by low-frequency wave energy (figure 10), a mean wave direction from the south (figure 11, upper panels) and low to moderate (6-12 m/s) winds from a southeasterly direction (figure 12), suggesting that the wave field is swell dominated.

Suppressed –Generation (SG) events

For these events, modeled wave heights are higher than observed (figure 9, examples are marked by asterisks), and the discrepancy is, in the majority of cases, smaller in the nearshore and more pronounced on the shelf. Mean wave directions are predominately from the west (figure 11), while winds come from land (figure 12) at speeds between 12-15 m/s, indicative of fetch-limited, wind-forced conditions. This implies that during these events the expected wind-wave growth, which should increase from onshore to offshore, is not reflected in the observations.

4.1 Propagation-Damping (PD) events

Wave heights

For PD events, the decrease in wave height from intermediate depths to shallow water is greater for the observations than is predicted by the model (figure 13). Additionally, differences between transects become apparent as observed wave heights are repeatedly lower on the central transect relative to wave heights on the western transect (figure 9). The latter could be due to a thicker mud layer near the central transect (5-10 cm of soft mud and 1-2 cm of very soft fluid mud on the central transect compared to < 5 cm of soft mud and < 1 cm of very soft fluid mud on the western transect) [Trainor, 2009, and references therein].

Energy dissipation

Wave height comparisons only identify local changes, which might be caused by shoaling and refraction and are not necessarily a result of the mud. To identify energy losses and to quantify the mud-induced dissipation, it is essential to examine the changes in wave energy flux (as opposed to wave heights) across the shelf. The cross-shore energy flux gradient is calculated between stations pv2 and pv4 on the western transect, between stations pv7 and pv9 on the central transect, and between nearshore stations n16 and n04 (figure 7). Cross-shore here is defined to be 10° from true North.

The total energy flux ($\hat{F}$) is calculated by

$$\hat{F} = \int_{0.04}^{0.25} F(df) \quad (5)$$

where the flux (F) is given by

$$F(f) = \rho g c_g(f) \cos\theta(f) S(f) \quad (6).$$

Group speed (c_g), direction (θ) and variance density spectrum (S) are functions of f as well; ρ and g are (constant) density and gravitational acceleration, respectively. Equation (5) is used to compute the flux from the modeled wave spectra at the same locations as the observations, and the flux gradients are estimated from observations and model through finite-differencing between stations. If we assume that the wave field is stationary, the bathymetry is one-dimensional, and that the model – apart from the influence of the mud – is 'exact', then we can estimate the mud-induced energy losses through

$$\frac{dF^{(\mathrm{obs})}}{dx} - \frac{dF^{(\mathrm{mod})}}{dx} \approx S_{\mathrm{mud}} \quad (7).$$

Integrated observed energy flux gradients for the shelf stations exhibit consistently higher dissipation rates for the observations throughout the time-series (figure14 and 15, upper panels), indicative of mud-induced damping in these intermediate water depths. Overall, dissipation rates are lower for the central transect, probably due to generally lower wave energies. Unfortunately, observations in the nearshore are less clear (figure 16) since data is missing at times due to high noise levels, and observations show erratic variations of energy flux gradients. In addition, the spectrum is dominated by high frequencies inshore that are not captured by our defined frequency range (0.04 Hz – 0.25 Hz). However, like the shelf stations, the nearshore experiences on average higher-than-predicted dissipation rates.

Integration of the energy flux gradient over the low-frequency and the high-frequency range separately shows (figures 14-16, middle and lower panel) that dissipation occurs mostly in the long-wave range up to 0.2 Hz. In fact, dissipation is greatest near the peak of the spectrum (figure 17, left column), as is also observed in the model-predicted dissipation. Dissipation of short waves seems to be relevant only in the period around March 17th, the time leading up to the most energetic event over the observational period (figures 14 and 15, lower panels).

Energy flux gradients, plotted in frequency-space and time (figures 18-20), show excellent qualitative and good quantitative agreement between observations (upper panels) and model (middle panels), although the model lacks the observed dissipation of higher frequencies. Evident is the fact that dissipation invariably takes place in the energetic range of the spectrum (lower panels).

4.2 Suppressed-Generation (SG) events

Wave heights

During SG events, the model overpredicts wave heights with the discrepancy increasing with distance offshore. These events coincide with strong winds from an offshore direction (shore normal is defined to be 10° from true north) (figure 12). This suggests that model overpredictions are caused by an incomplete representation of wind-wave growth during offshore and slanting fetch conditions over mud. Comparisons of measurements at all stations (including pa's and all nearshore sensors) show (figure 21.a) that wave heights are systematically overpredicted during offshore winds (340° - 20°, where 0° is assumed to be shore normal) and slanting fetch from the west (300° - 340°) (figure 21.b). The agreement is better during slanting fetch from the east (20°-60°) (figure 21.c) and winds from the south (150° -230°) (figure 21.d).

Generation

The discrepancy between modeled and observed wave heights during SG events can be explained by slower than predicted wind-wave growth. In fact, the majority of observed energy flux gradients show either low generation, or no generation at all (figures 14, 15, 18, and 19). Generation for the central transect is even less (with the exception of the event on and after February 26th).

Observed variance densities show (figure 23, 24 and 25, left column) increases in the short-wave range from onshore to offshore, but generation occurs at a lower rate than the model predicts. Modeled source terms illustrate (figure 22, 23, and 24, middle column) the expected generation (black curve) and the non-linear (four-wave) energy transfer (blue curve) toward lower frequencies. In contrast, predicted and observed wave directions (figure 22 and 23, right column) agree fairly well, suggesting that although the wave field is wind-forced, the energy input to the waves is largely reduced when compared to what would be expected over a sandy seafloor. Predicted and observed wave directions deviate from each other on March 24th (figure 24, right column), probably caused by the repeated shift in wind direction between northeast and northwest.

Although some of the discrepancies between model and observations during SG events may be caused by limitations of our model implementation (these are discussed in detail in chapter 6), the observed suppression of wave growth suggests that the model is missing important physics. In particular, during SG events, wind speeds are fairly high (12-15 m/s) which, under "normal" conditions, in a young sea state like this, would drive considerable wave growth [see e.g. Hasselmann et al., 1973; Janssen, 1991]. However, in our observations wind-wave generation is very small or absent entirely. Consider for instance the observations on March 24th, when wind speeds are about 12 m/s, coming from a northerly direction (figure 12). Observed energy flux gradients for this time show barely any generation (figures 14 and 15), and significant wave heights reach no more than 30 cm (figure 9) after about 12 km of fetch. We suspect that this lack of wave generation in the nearshore is associated with the presence of mud in the water column, somehow prohibiting efficient transfer of momentum from the wind to the waves.

5. Turbidity

For a rough estimate of suspended sediment concentrations in the water column, we use the normalized backscatter intensity from the ADCPs at stations pv4 (figure 25). We do not treat this observation as a quantitative proxy for sediment concentrations, but expect that relative changes in backscatter intensity are associated with relative changes in sediment concentrations, and can be used to investigate a possible correlation between increased sediment concentration, wave attenuation, and reduced generation.

From our observations, it appears that sediment resuspension events are initialized by current speeds (figure 26) which often exceed the critical speed for resuspension of ~ 30 cm/s [Lesht and Hawley, 1987; Sheremet et al., 2005]. The local wind field is the main driver for the currents (black lines in figure 26), and the high correlation between currents and increased backscatter (figure 27), indeed suggest that the currents are involved in the sediment resuspension.

PD and SG events coincide with increased sediment concentrations at ~ 1 m above the bottom (figure 25), and backscatter intensities throughout the water column appear to be particularly elevated during suppressed generation (SG) events (figure 28, white stars). Also notice the elevated backscatter signals around and after March 17^{th}, where, for a period of several days, no generation was observed while dissipation rates where higher than predicted (figure14 and 15).

On the other hand, low sediment concentrations during the time from February 21^{st} to February 26^{th} and on March 16^{th} (figures 25 and 28) could explain the good agreement between modeled and observed wave heights in the nearshore. Model and observations agree well on March 16^{th} (figure 9), which is an exception during a time that is dominated by consistently over-predicted wave heights in the nearshore.

The correlation between wind-driven currents, sediment suspension, and suppressed generation is striking and supports the idea that the presence of suspended mud in the water column suppresses the momentum transfer from the wind to the waves. At present, this physical mechanism of this interaction of the mud with the wave field is not well understood and further research is needed to identify the physical processes through which such damping can take place.

6. Discussion

Overall, the agreement between the model, with sandy-bottom settings, and the observations of wave evolution across the muddy Louisiana inner shelf is remarkably good. This suggests that 1) mud damping appears is episodic, and 2) the model implementation of wave and water level boundary conditions is adequate to capture the principal wave dynamics in this nearshore region.

Peculiar is the underprediction of wave energy on the inner shelf as seen during swell-dominated conditions; however, the same behavior has also been reported in sandy coastal environments [e.g. Rogers et al., 2003; Van der Westhuysen et al., 2007; Van Vledder et al., 2010], and could possibly be due to model errors, and not due to mud.

Model implementation

Boundaries

The southern boundary is initialized with observations from two stations, both on the eastern side of our domain and both in relatively shallow water. This may have introduced boundary errors, especially for the (deeper) western transect.

We used 1D-model runs to provide high-resolution (and smooth) boundary conditions on the sides of our domain to avoid boundary effects (leaking, shadowing). Although a considerable improvement to either not specifying the boundary, or using a single nearby observation, this approach may still not be accurate for all conditions, in particular for conditions where the wind is blowing along the coast. This situation can be improved by nesting the computational domain covering the observational area into a larger-scale, regional model, which would also improve the southern boundary condition. This has not been pursued here but will be considered in a follow-up study.

Wind forcing

We have argued, based on our observations, that the presence of mud appears to suppress wave generation by wind. This of course critically depends on the wind-input to the model, and whether wind fields are sufficiently accurate and resolved.

We assumed a homogenous wind field in the area of interest. The comparison of the WHOI-buoy with two other buoys in the area suggests that the averaged wind is indeed fairly homogenous. Even so, metrological observations (and model output) were only available at a limited number of locations, and spatial variability of wind gustiness on wind-wave growth is not considered in SWAN (The WISE Group, 2007). Further, we have scaled the wind fields to account for the effects of decreased roughness length over water. However, these corrections cannot be validated here since only a single meteorological observation buoy is present in our area of interest. However, comparisons of the scaled winds to observations from a nearby NDBC weather buoy suggest that the roughness down-scaling is an improvement. In any case, model runs without wind-scaling show similar results (not shown), which suggests that the model is not overly sensitive to variations (or errors) in the roughness scales. Despite the difficulties in providing accurate wind information to the model, we expect that the wind input is not a principal source of error.

Currents

In the present model implementation, we ignored the influence of coastal currents. However, our analysis shows that current speeds often exceed 20 cm/s. For the relatively high-frequency wind waves in this area, such currents could be important.

Triads

We have ignored triad (three-wave) interactions, which are particularly important in shallow water. We have chosen to ignore them since 1) we doubt that the triad implementation in the SWAN version used in this study would actually improve the realism of the model, and 2) most of our comparisons were made in intermediate depth where triad interactions would be (very) weak.

Slanting fetch

It is possible that the differences between observations and model results during slanting-fetch conditions reflect the general difficulty of modeling wave growth under such conditions in third-generation wave models [e.g. Ardhuin et al. 2007], and are therefore not specific for this muddy environment. However, in our comparison we did not detect any of the characteristic shifts in wave directions, as seen in conventional slanting-fetch conditions [Ardhuin et al. 2007]. In fact, mean wave directions across the spectrum agree generally very well for most cases, with the exception March 24th, when the wind field was highly variable.

Regardless of the above, several times during the observations, strong wind forcing was present but no wave growth was observed. This leads us to believe that the differences in wave generation between observations and model are associated with a reduced effectiveness of the atmospheric boundary layer to transfer momentum (and thus energy) into the ocean's surface (in the form of wind waves). In fact, a model run in which the wind was turned off shows much better agreement with the observations than when the wind was turned on with the correct wind field (figure 29).

Our observations suggest that the occurrence of SG events is correlated to the events of enhanced turbidity in the water column, but the particulars of this will need further study.

7. Conclusion

The goal of this study was to investigate the effect of mud across the inner Louisiana shelf, and to identify the principal mechanisms that affect the nearshore wave energy balance due to the presence of mud on the seafloor. We have implemented a conventional wave model with settings suitable for a sandy shelf environment, to identify the differences between a sandy environment and the Louisiana mud coast. From our analysis, we have successfully combined two new datasets, and through detailed analysis identified two principal classes of events: 1) swell-dominated events (Propagation-Damping events), characterized by damping of energy in the energetic range of the spectrum, preferential toward lower frequencies, and 2) events in which the presence of the mud appears to strongly suppress the growth of wind sea (Suppressed Generation events).

Overall, the model-data comparison is surprisingly good, apart from isolated events, which suggests that strong wave-mud interaction is episodic (consistent with earlier findings), and that the presence of mud can act as a growth suppressor.

References

Allison, M., G. Kineke, E. Gordon, and M. Goñi (2000), Development and reworking of a seasonal flood deposit on the inner continental shelf off the Atchafalaya River, *Continental Shelf Res. 20*, 2267–2294.

Ardhuin, F., T. H. C. Herbers, G. P. van Vledder, K. P. Watts, R. Jensen, and H. C. Graber (2007), Swell and slanting-fetch effects on wind wave growth, *J. Phys. Oceanogr.*, 37, 908–931, doi:10.1175/JPO3039.1.

Booij, N., Ris, R.C., and L.H. Holthuijsen (1999). A third-generation wave model for coastal regions. 1. Model description and validation. *J. Geophys. Res.*, 104(C4), 7469-7666.

Bouws, E., and Komen, G.J. (1983). On the balance between growth and dissipation in an extreme, depth limited wind-sea in the southern North Sea, *J. Phys. Oceanogr., 13,* 1653-1658.

Dalrymple, R.A., and P. L-F. Liu (1978), Waves Over Soft Muds: A Two-Layer Fluid Model, *Journal of Physical Oceanography*, *8*, 1121-1131.

Draut, A., G. Kineke, D. Velasco, M. Allison, and R. Prime (2005), Influence of the Atchafalaya River on recent evolution of the chenier-plain inner continental shelf, northern Gulf of Mexico, *Continental Shelf Res.* 25, 91–112.

Elgar, S., and B. Raubenheimer (2008), Wave dissipation by muddy seafloors, *Geophysical Research Letters, 35*, L07611, doi:10.1029/2008GL033245.

Gade, H. (1958). Effects of a non-rigid, impermeable bottom on plane surface waves in shallow water. *J. Mar. Res, 16*, 61-82.

Garcia-Garcia, A., T. T. Janssen, T. H. C. Herbers, D. Alden, A. Orange, D. Orange, P. Jessen, S. Kawamoto, and P. Harvey (2011) A geophysical baseline for the Fluid-Mud MURI site, west of Atchafalaya Bay, under review at *Geo-Mar. Lett.*

Hasselmann, K., T.P. Barnett, E. Bouws, H. Carlson, D.E. Cartwright, K. Enke, J.A. Ewing, H. Gienapp, D.E. Hasselmann, P. Kruseman, A. Meerburg, P. Mueller, D.J.Olbers, K. Richter, W. Sell, and H. Walden (1973). Measurements of wind-wave growth and swell decay during the Joint North Sea Wave Project (JONSWAP). *Dtsch. Hydrogr. Z. Sup.* A8(12), 95

.

Janssen, P.A.E.M., (1991). Quasi-linear theory of wind wave generation applied to wave forecasting. *J. Phys. Oceanogr.* 21, 1631-1642.

Johnson, H.K. (1999). Simple expressions for correcting wind speed data for elevation, *Coastal Engineering*, Volume 36, 3, Pages 263-269, ISSN 0378-3839, DOI: 10.1016/S0

Lesht , B.M., and N. Hawley (1987). Near bottom currents and suspended sediment concentration in southeastern Lake Michigan. *J. Great Lakes Res.* 13:375–383.

Ng, C. O. (2000), Water waves over a muddy bed: a two-layer Stokes' boundary layer model, *Coastal Engineering*, *40*(3), 221–242.

Rogers, W. E. and T. Holland (2009) A study of dissipation of wind-waves by mud at Cassino Beach, Brazil: prediction and inversion. *Cont. Shelf Res.*, 29, 676-690.

Rogers, W.E., Hwang, P.A., and D.W. Wang (2003). Investigation of wave growth and decay in the SWAN model: three regional-scale applications. *J. Phys. Oceanogr.* 33, 366–389.

Sheremet, A., A. J. Mehta, B. Liu, and G. W. Stone (2005), Wave–sediment interaction on a muddy inner shelf during Hurricane Claudette, *Estuarine, Coastal and Shelf Science*, *63*(1-2), 225–233.

Sheremet, A., and G. W. Stone (2003), Observations of nearshore wave dissipation over muddy sea beds, *Journal of Geophysical Research*, *108*(C11), 3357.

Svendsen, I.A. (2006), *Introduction to Nearshore Hydrodynamics, Advanced Series on Ocean Engineering* vol. 24, World Scientific, Singapore

Taylor, P.A. and R. J. Lee, (1984) Simple guidelines for wind speed variations due to small-scale topographic features *Clim. Bull.* 18, 3-32

The WISE Group (2007): Wave modelling: The state of the art, *Progr. Oceanogr.*, 75, 603–647.

Trainor, L.T., (2009), Field observations and SWAN model predictions of wave evolution in a muddy coastal environment, MSc dissertation, Naval Postgraduate School, Monterey 73p.

Van der Westhuysen, A.J., M. Zijlema and J.A. Battjes (2007): Nonlinear saturation-based whitecapping dissipation in SWAN for deep and shallow water, *Coast. Engng.*, 54, 151-170

Van Vledder, G., Zijlema, M., and L. Holthuijsen (2011). Revisiting the JONSWAP bottom friction formulation. *Proceedings Of The International Conference On Coastal Engineering*, 1(32).

Wells, J.T., and G.P. Kemp (1981). Atchafalaya mud stream and recent mudflat progradation: Louisiana chenier plain. *Transactions—Gulf Coast Association of Geological Societies* 31, 39–46.

Winterwerp, J.C., de Graff, R.F., Groeneweg, J., and A.P. Luijendijk (2007). Modelling of wave damping at Guyana mud coast. *Coastal Eng., 54,* 249-261.

Yan, L. (1987): An improved wind input source term for third generation ocean wave modeling, Scientific report WR-No 87-8, De Bilt, The Netherlands

Western transect, shelf				
Station name	Latitude (Deg. North)	Longitude (Deg. West)	Depth (MSL) (m)	Notes
dw1	29.44418	92.63243	13.3	available only until 03/05/2008
pv2	29.47670	92.62452	11.3	
pa3	29.50370	92.60323	9.6	
pv4	29.52315	92.59897	8.3	ADCP used
pa5	29.53943	92.59457	6.4	not recovered
pa6	29.55330	92.59190	4.6	misplaced by fisher boat, used since depth seems ok
Western transect, nearshore				
Station name				
n16	29.57543	92.56051	4.0	
n15	29.57413	92.56084	3.9	
n14	29.57273	92.56110	3.7	
n13	29.57142	92.56120	3.6	
n12	92.56165	29.56999	3.4	
n11	92.56195	29.56851	3.2	
n10	92.56222	29.56727	3.0	not recovered
n9	92.56245	29.56600	2.8	
n8	92.56289	29.56446	2.5	
n7	92.56314	29.56311	2.2	
n6	92.56331	29.56170	2.0	
n5	92.56358	29.56041	1.9	
n4	92.56389	29.55896	1.7	
n3	92.56400	29.55764	1.4	
n2	92.56444	29.55618	1.3	
n1	92.56473	29.55460	1.3	moved, excluded from analysis

Central transect				
Station name				
pv7	29.42407	92.49975	10.9	
pa8	29.45290	92.49433	9.9	
pv9	29.49110	92.47482	8.3	
pa10	29.51773	92.46267	6.8	displaced by fishing vessel , excluded from analysis
pa11	29.52860	92.45878	5.7	not recovered
Eastern transect				
Station name				
dw12	29.32995	92.48897	10.9	
pv13	29.32675	92.43167	8.8	
pa14	29.30833	92.38973	7.6	
pa15	29.30785	92.31747	6.8	
pv16	29.29388	92.26530	5.5	

Table 1. Station locations in latitude and longitude, depths, and notes for missing or excluded sensors. dw are Datawell Waverider buoys, pv are shelf Vector pressure-velocity sensors, pa are pressure recorders, ADCP are Acoustic Doppler Current Velocimeters; the n* are the collocated pressure and velocity sensors in the nearshore.

Sensor code	**Length time series(min)**	**Sampling rate (Hz)**	**Block length**	**Degree of freedom**	**Frequency resolution (Hz)**
dw	70	1.28	84	192	0.0152
pv, pa	68.2	2	128	192	0.0156
adcp	34	1	64	96	0.0156
n*	51.2	2	96	192	0.0208

Table 2. Length of time series, sampling frequencies, number of blocks and resulting degrees of freedom using a Hamming window with 50% overlap, and frequency resolution. dw are Datawell Waverider buoys, pv are shelf Vector pressure-velocity sensors, pa are pressure recorders, adcp are Nortek Acoustic Doppler Current Velocimeters; the n* are the collocated pressure and velocity sensors in the nearshore.

	1D	2D
Computational grid	500 (north-south)	1200 (east-west) x 500 (north-south)
Computational resolution	272.8 m	338.1 m x 272.8 m
Geographic resolution	91.6 m	72.5 m x 91.6 m
$\Delta\ \theta$	10°	10°
Computations	Every 10 minutes	Every 10 minutes
Physics	GEN 3, Westhuysen Generation by wind White-capping Depth induced wave breaking (gamma = 0.73) Bottom friction (JONSWAP = 0.038 m^2s^{-3}) Quadruplets (DIA)	GEN 3, Westhuysen Generation by wind White-capping Depth induced wave breaking (gamma = 0.73) Bottom friction (JONSWAP = 0.038 m^2s^{-3}) Quadruplets (DIA)
Boundaries	Eastern boundary initiated by pv16 (hold constant for 4 hrs). Western boundary initiated by dw12.	South, initiated by dw12 and pv16 (hold constant for 4 hrs). East, from 1D runs, west, from 1D runs.
Propagation scheme	BSBT	BSBT

Table 3. Grid resolutions and physics for 1D and 2D non-stationary SWAN runs.

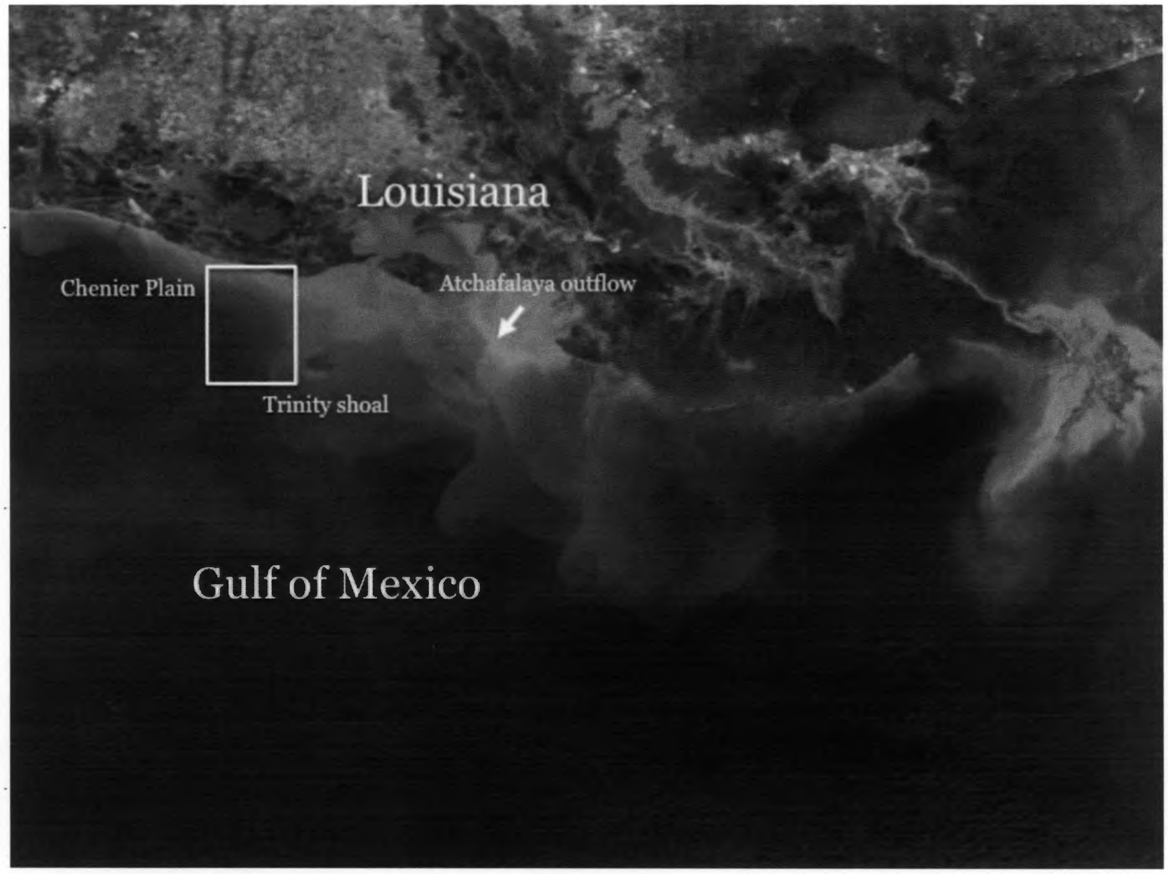

Figure 1. Satellite image overlaid by google earth imagery showing the Louisiana coast, Chenier plain, and the Atchafalaya outflow. The white square indicates the study area.

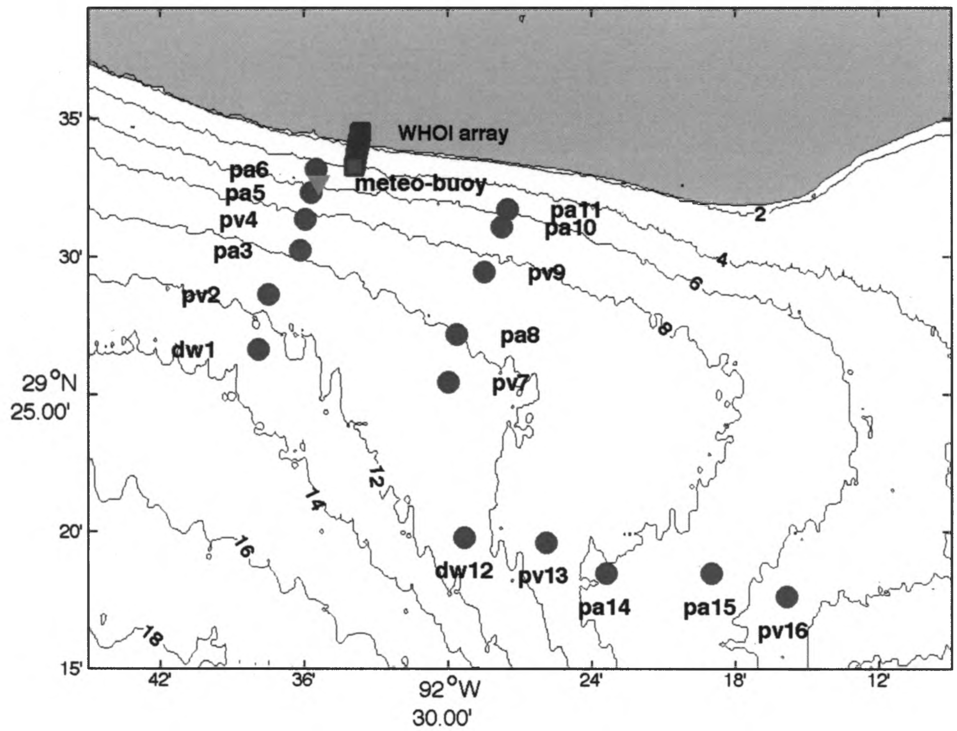

Figure 2. Overview of sensor locations in the study area. Blue dots indicate the inner shelf stations (NPS/SIO) where dw-stations are Datawell Waverider buoys, pv are Nortek Vector pressure-velocity sensors, and pa are pressure recorders. Red dots show the WHOI nearshore array; the nearshore sensors are referenced in the text as n1, n2, ..., n16, in order of increasing depth. The green dot shows the approximate location of the meteorological buoy.

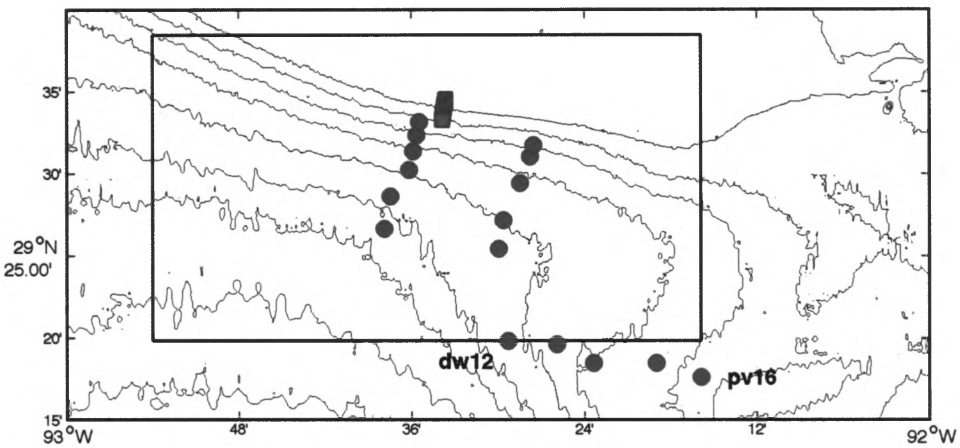

Figure 3. Shown are the margins of the bottom grid (whole area shown) and the computational grid (smaller area). Boundary conditions on the south side of the grid were initialized with dw12 and pv16, while 1D non-stationary runs on the eastern side were forced with information from pv16, on the western side with dw12.

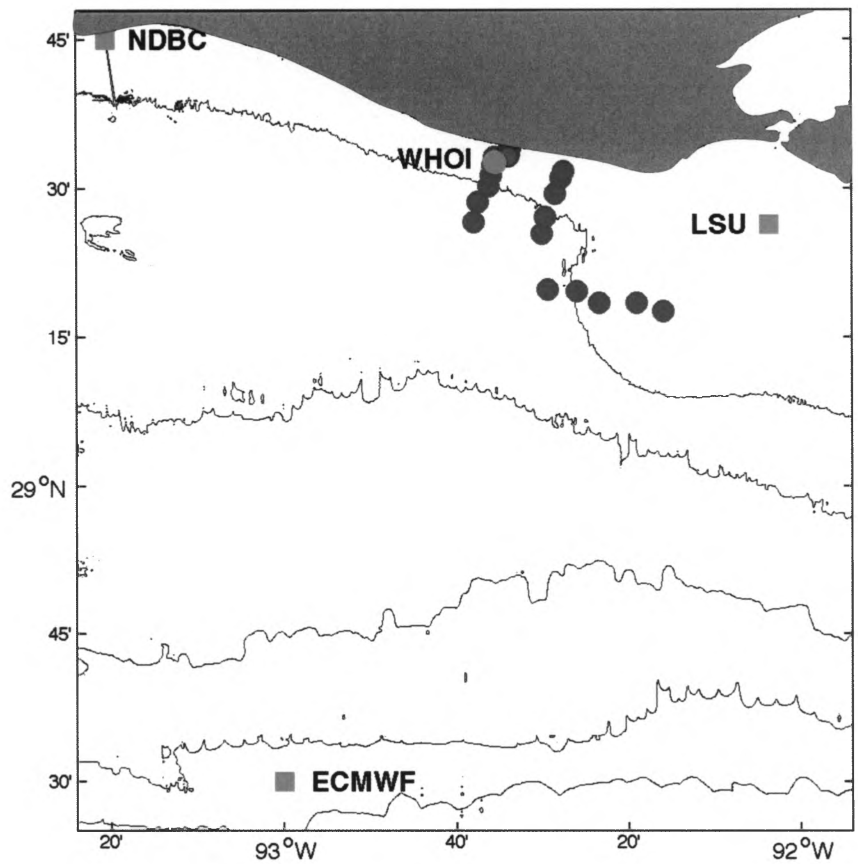

Figure 4. Position of meteorological stations and the position of the ECMWF-model output.

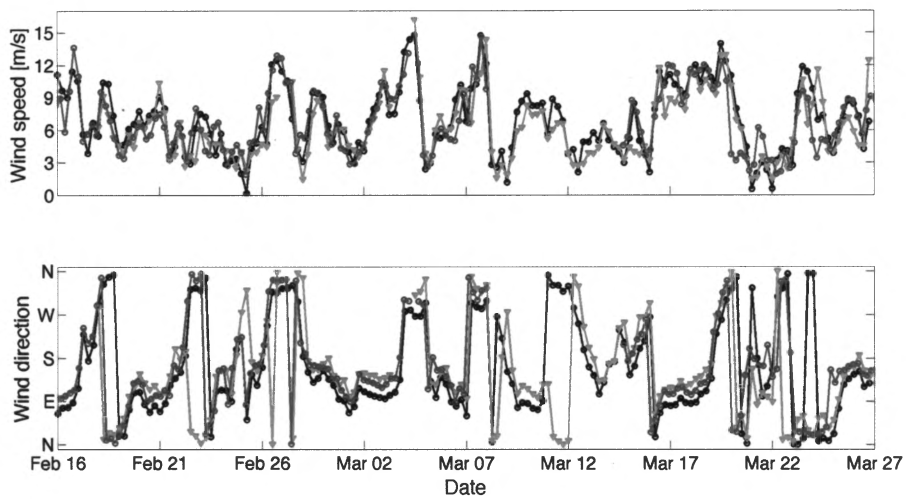

Figure 5. Comparisons of the WHOI buoy (black curve) with the LSU buoy (green curve) and the NDBC buoy (blue curve). Upper panel shows wind speed, lower panel shows wind direction.

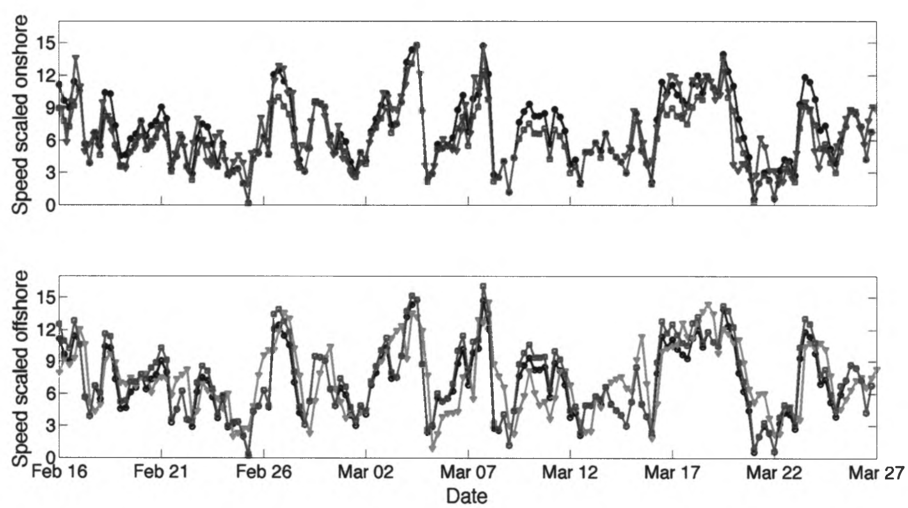

Figure 6. The upper panel shows the result of scaling the wind speed (blue curve) from the WHOI buoy (black curve) to the shoreline in a comparison with the onshore NDBC buoy (red curve). The lower panel shows the effect of scaling the wind speed (blue curve) to the latitude of the ECMWF output (green curve) from the WHOI buoy (black curve).

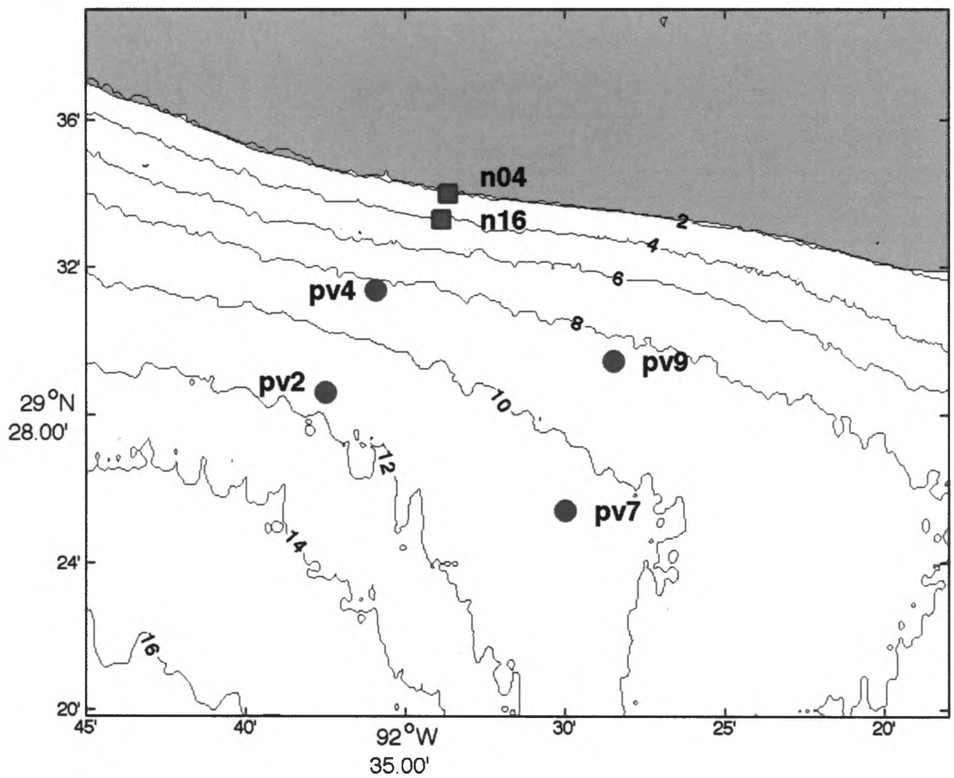

Figure 7 Station locations that are used for the time-series comparisons of wave heights (pv2, pv7, n16, and n04) and energy flux gradients.

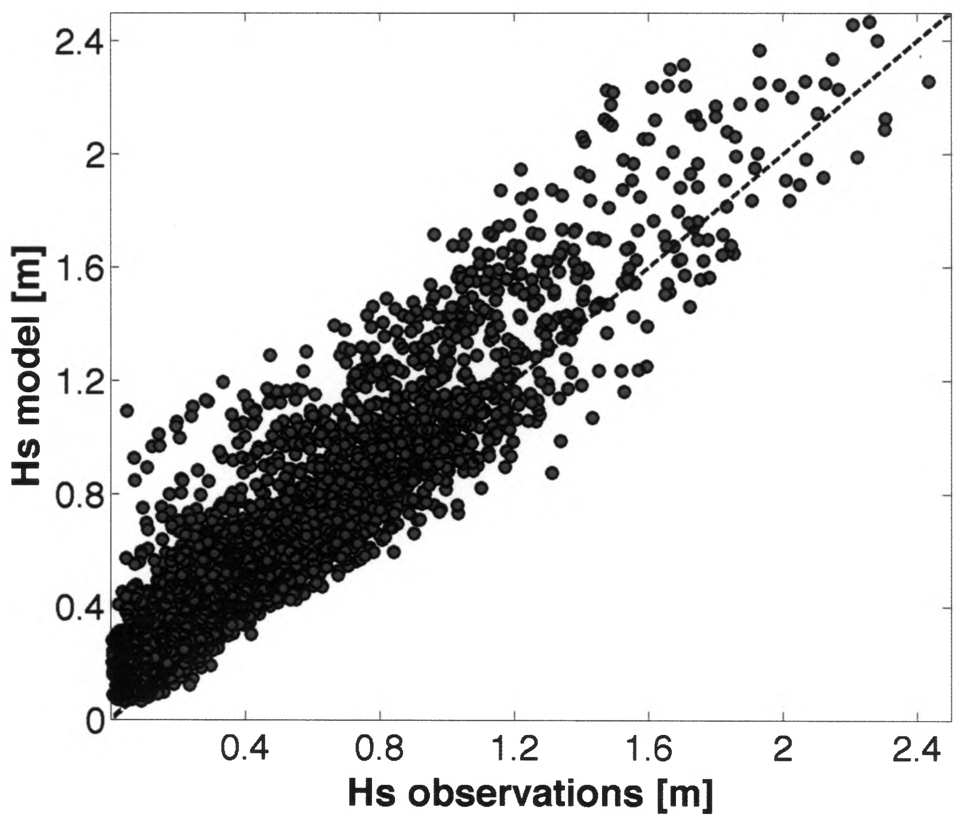

Figure 8. Scatter plot of modeled and observed wave heights for all stations. The black dashed line is perfect agreement (1:1).

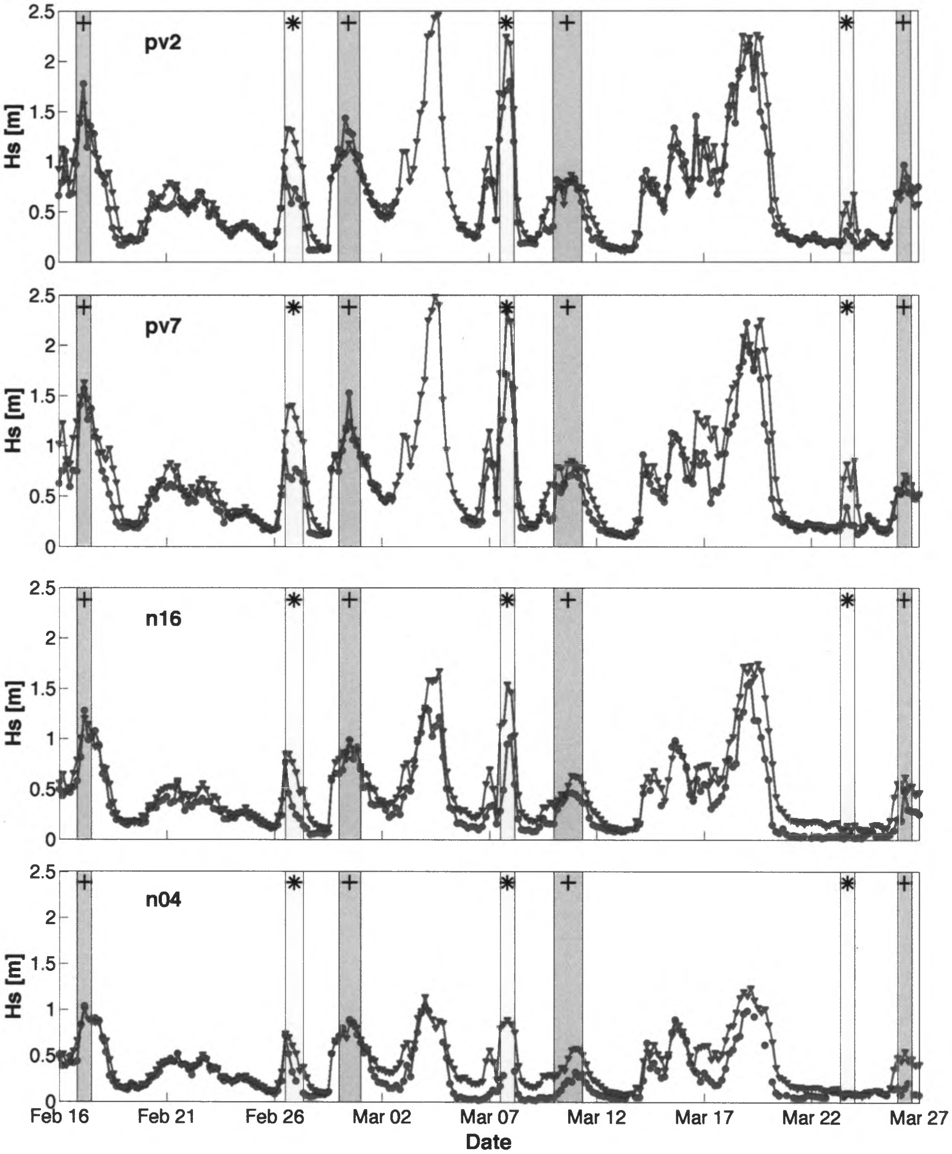

Figure 9. Comparison of observed (red line) and modeled (blue line) significant wave heights for sensors pv2, pv7, n16, and n04 (top to bottom). Observations are missing for the inner shelf stations (pv2 and pv7) from ~ March 2nd to March 5th due to instrument turn-around.
Crosses and grey highlighting indicate examples of PD events; asterisks and yellow highlighting show examples of SG events.

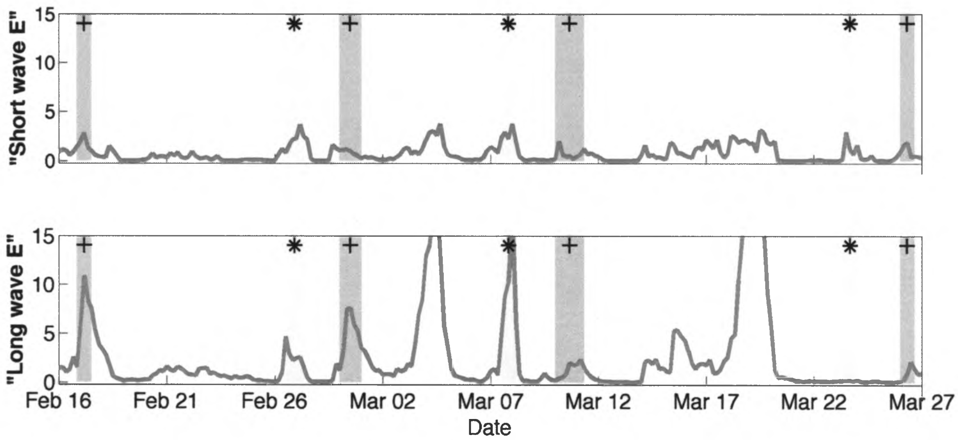

Figure 10. Upper panel: variance density in short wave range (0.2 – 0.25 Hz); lower panel: variance density in long wave range (0.04 – 0.2 Hz).

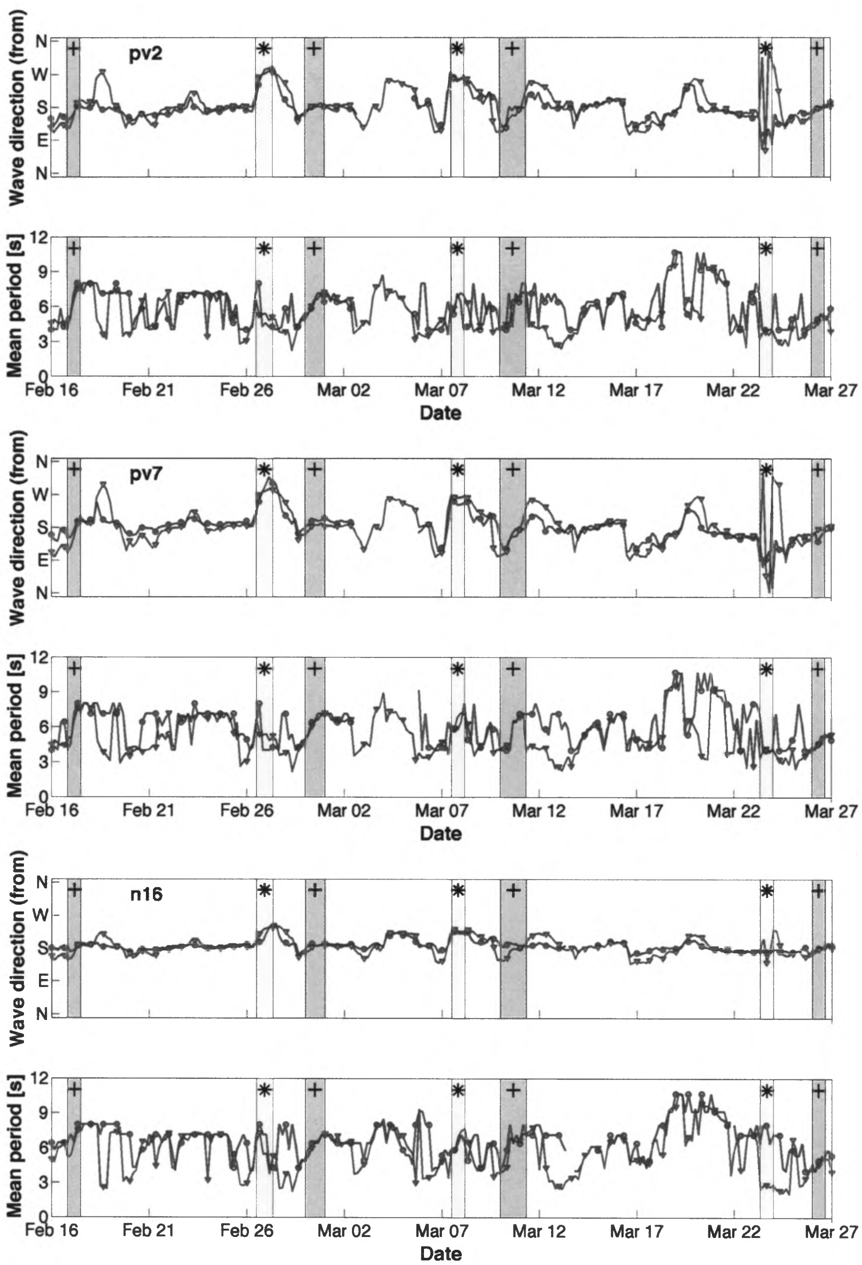

Figure 11. From top to bottom: sensors pv2, pv7, and n16.
Observed (red curve) and modeled (blue curve) mean wave direction (defined as the direction from) is shown in upper panels; the lower panels shows peak periods for observations (red curve) and model (blue curve).

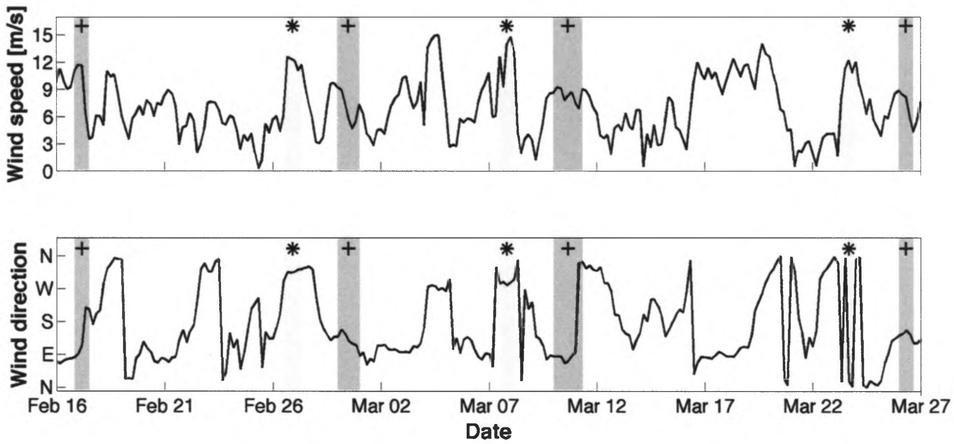

Figure 12. Wind speed (upper panel) and wind direction (lower panel) time series with highlighted PD (crosses, grey) and SG (asterisks, yellow) events.

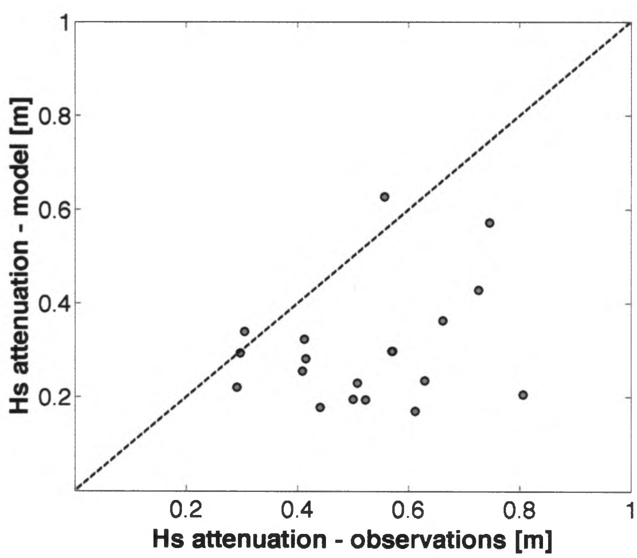

Figure 13. Scatter plot for PD events of modeled and observed wave height attenuation (difference between pv2 and n04), model over observations.

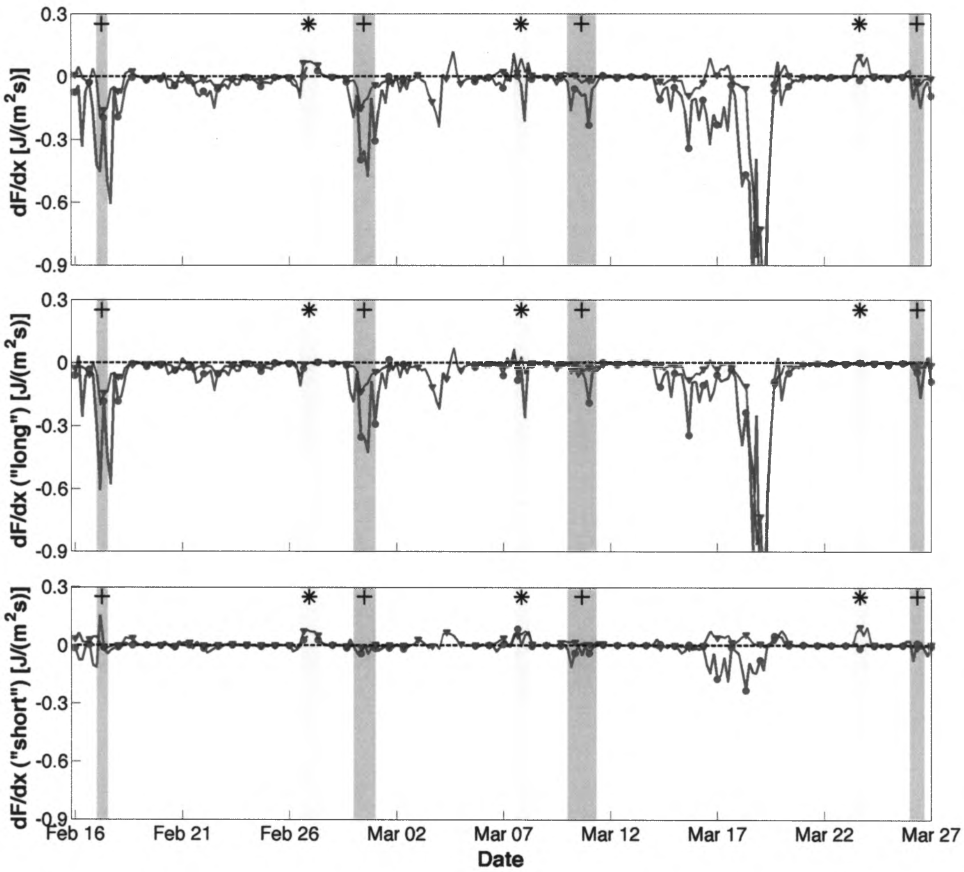

Figure 14. The upper panel shows the energy flux gradient for observations (red curve) and model (blue curve) between pv2 and pv4. Middle panel shows the same but for the long wave range (0.04-0.20 Hz). The lower panel shows the short wave range (0.20-0.25 Hz). Crosses and grey highlighting indicate PD events; asterisks and yellow highlighting show SG events.

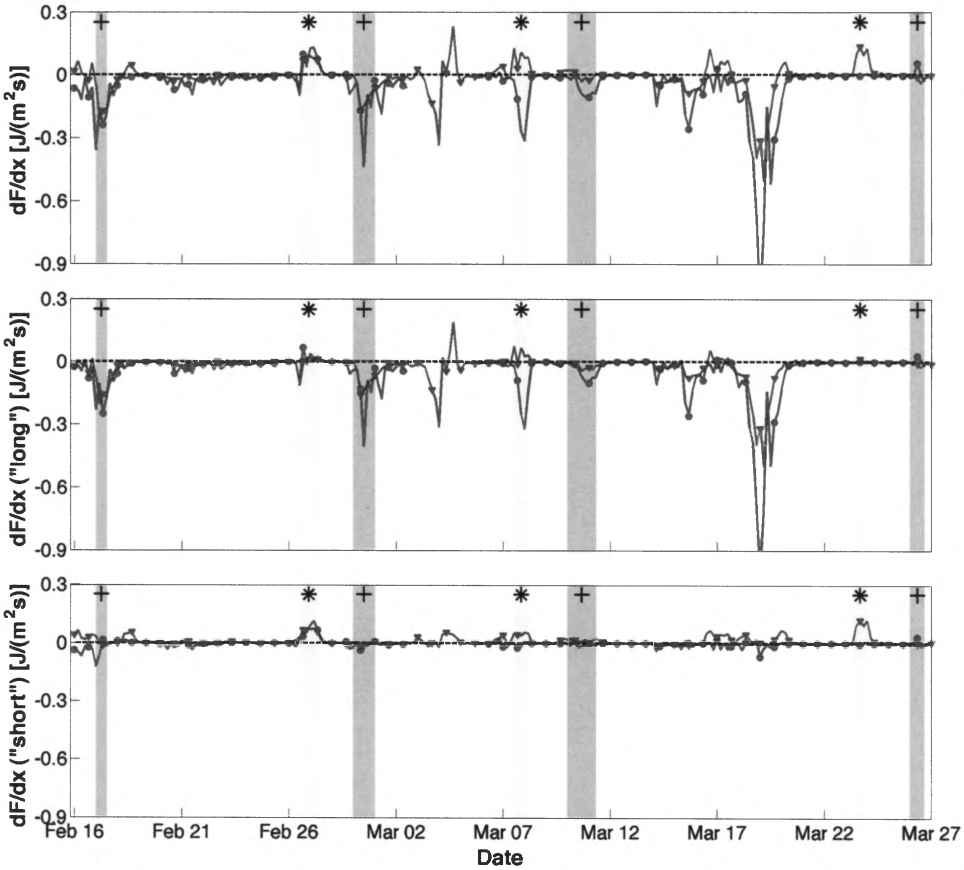

Figure 15. Same as figure 15 for the energy flux gradient between pv7 and pv9.

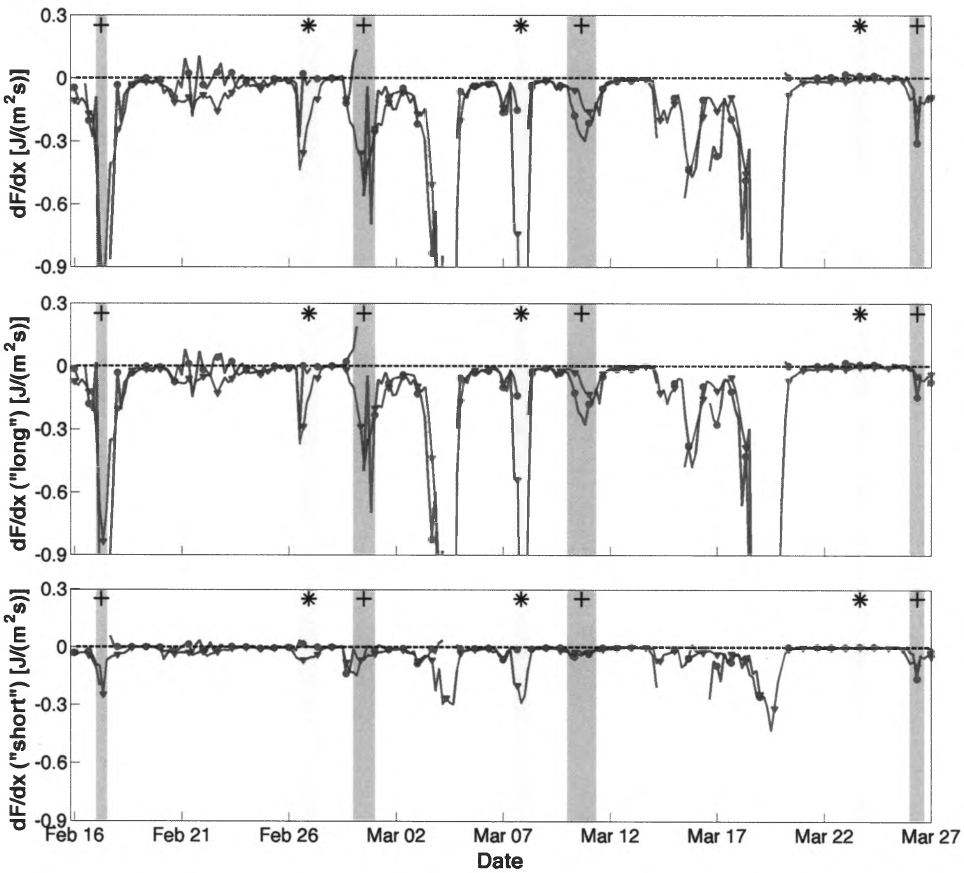

Figure 16. Same as figure15 for the energy flux gradient between n16 and n04.

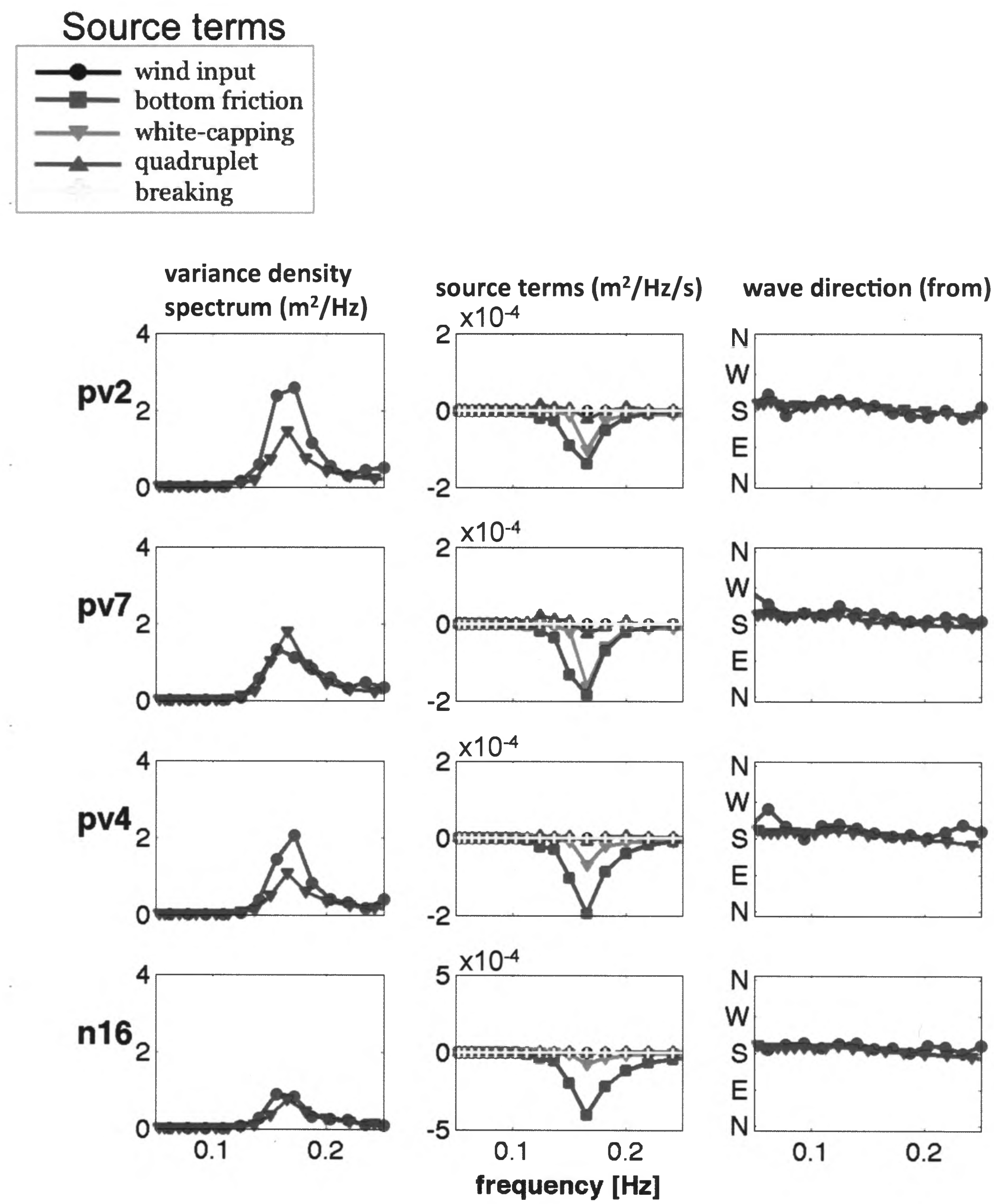

Figure 17. Left column shows the variance density spectrum for observations (red) and model (blue). Middle column shows SWAN source Right columns shows wave directions for observations (red) and model (blue).
Shown is February 17th for sensors pv2, pv7, pv4, n16, top to bottom.

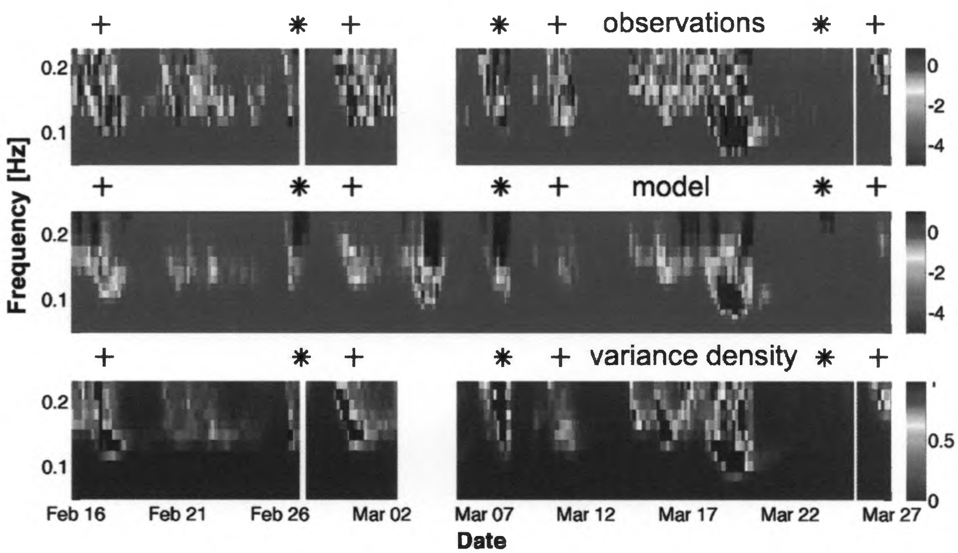

Figure 18. Shown, between pv2 and pv4, are the energy flux gradients for observations (upper panel), the energy flux gradients for the SWAN model (middle panel) and the observed mean variance density between these stations (lower panel). Crosses indicate PD events, asterisks indicate SG events.

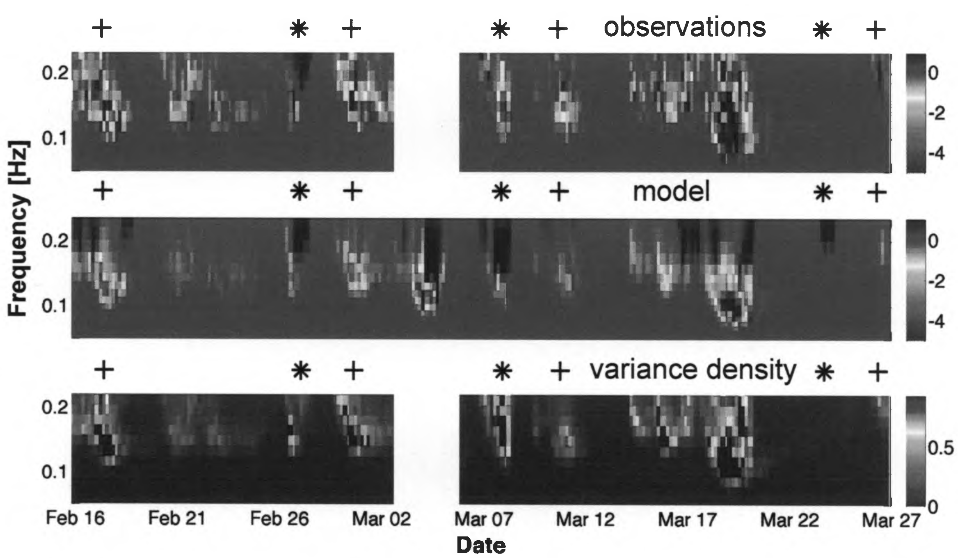

Figure 19. Same as figure 16, but the comparison shows results between pv7 and pv9.

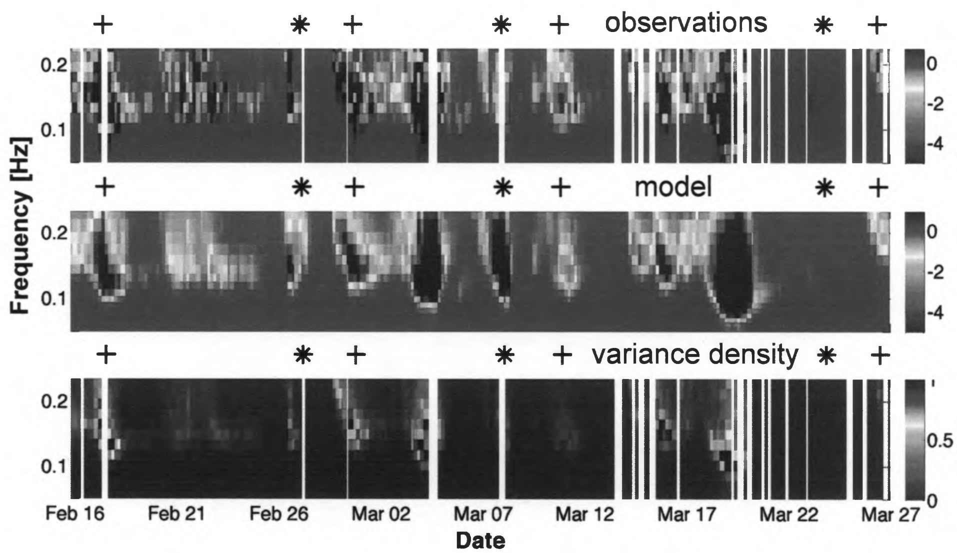

Figure 20. Same as figure 16, but the comparison shows results between n16 and n04.

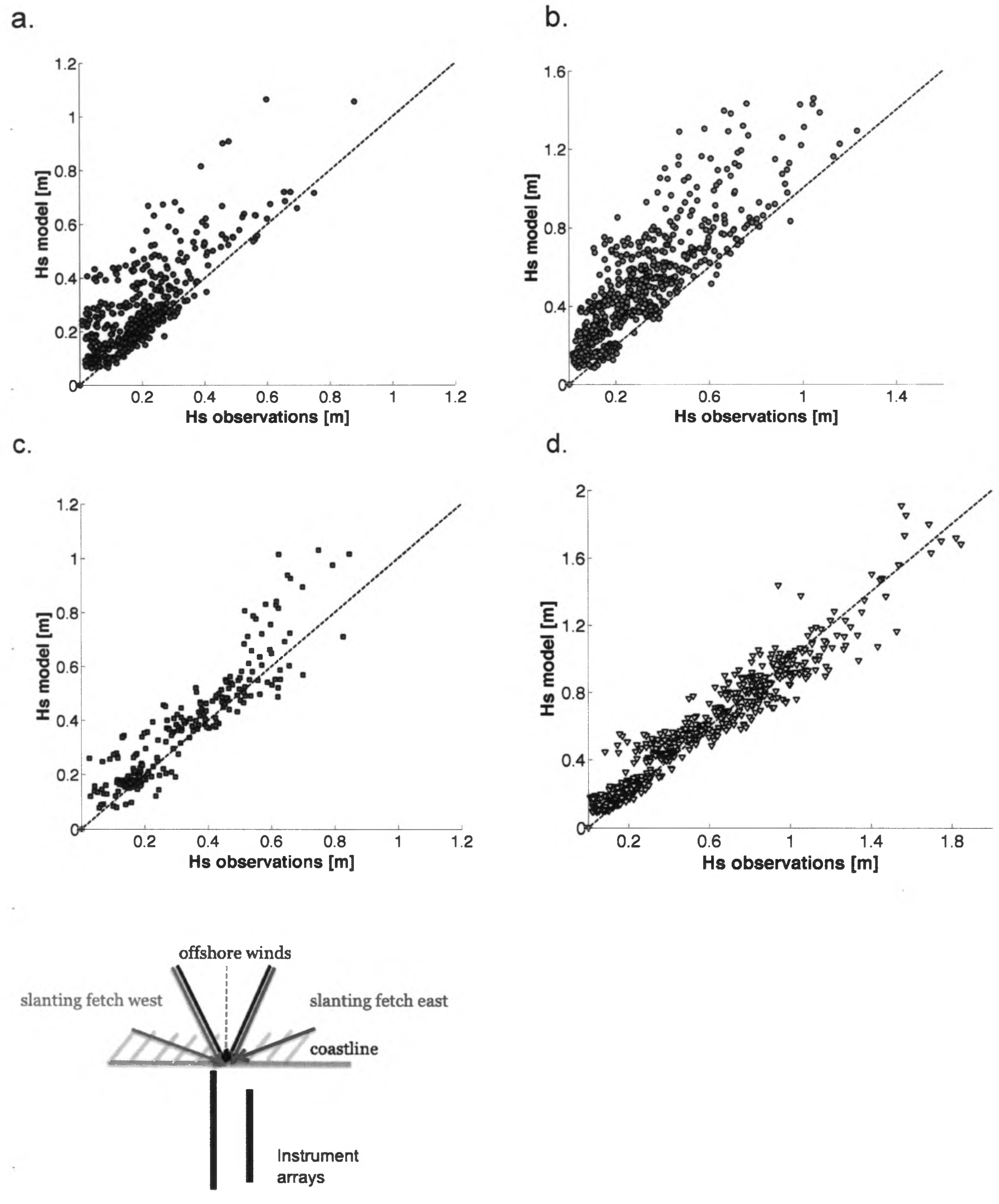

Figure 21. Modeled versus observed significant wave heights in different wind/swell conditions. The black dashed line is perfect agreement (1:1). a. offshore winds (340° - 20°, 0 is assumed to be shore normal, see schematic, b. slanting fetch from west (300°-340°),), c. slanting fetch from east (wind coming from 20°-60°), d. swell arriving from southerly (150°-230°) directions.

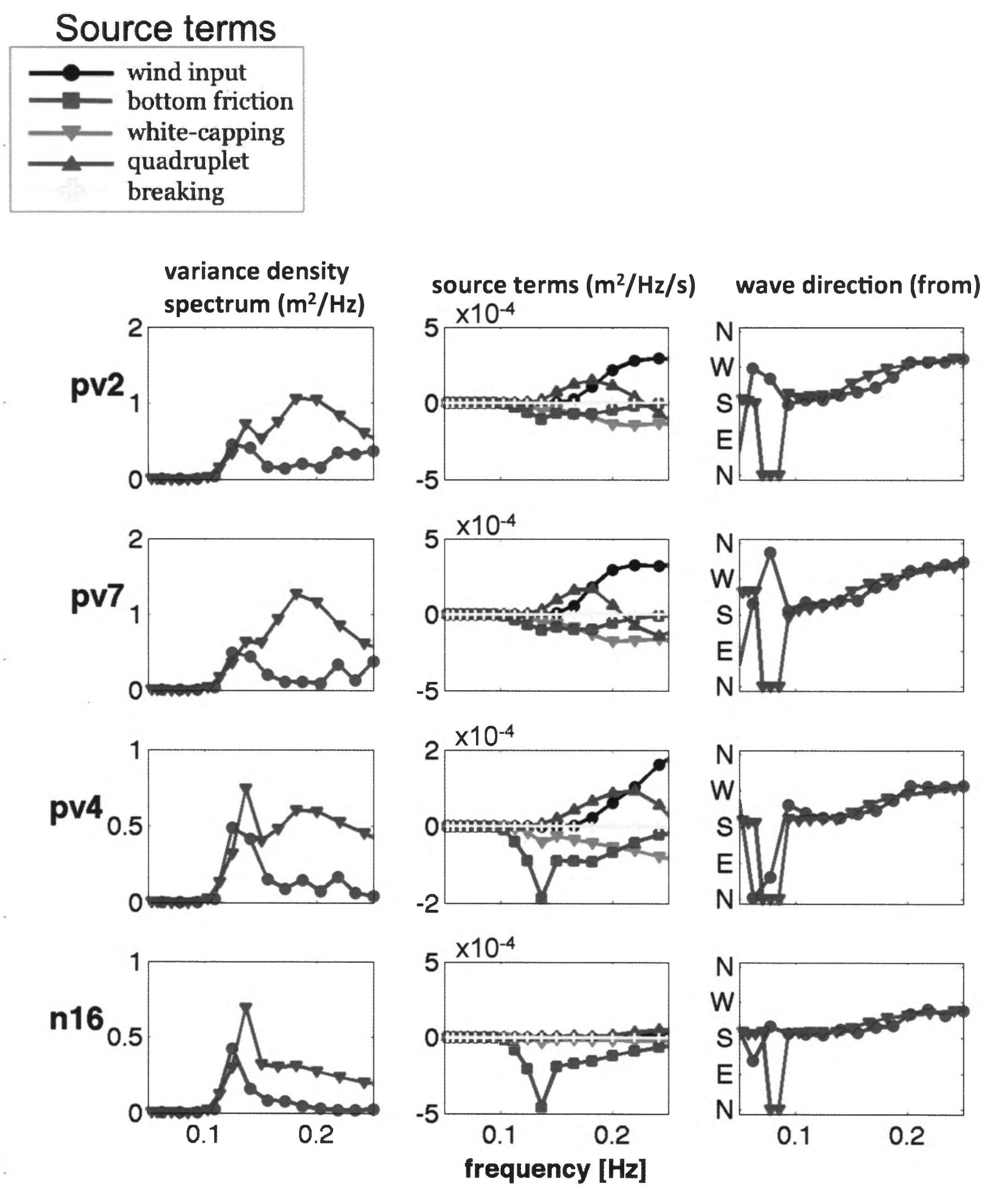

Figure 22. Left column shows the variance density spectrum for observations (red) and model (blue). Middle column shows SWAN source Right columns shows wave directions for observations (red) and model (blue).
Shown is February 26th for sensors pv2, pv7, pv4, n16, top to bottom.

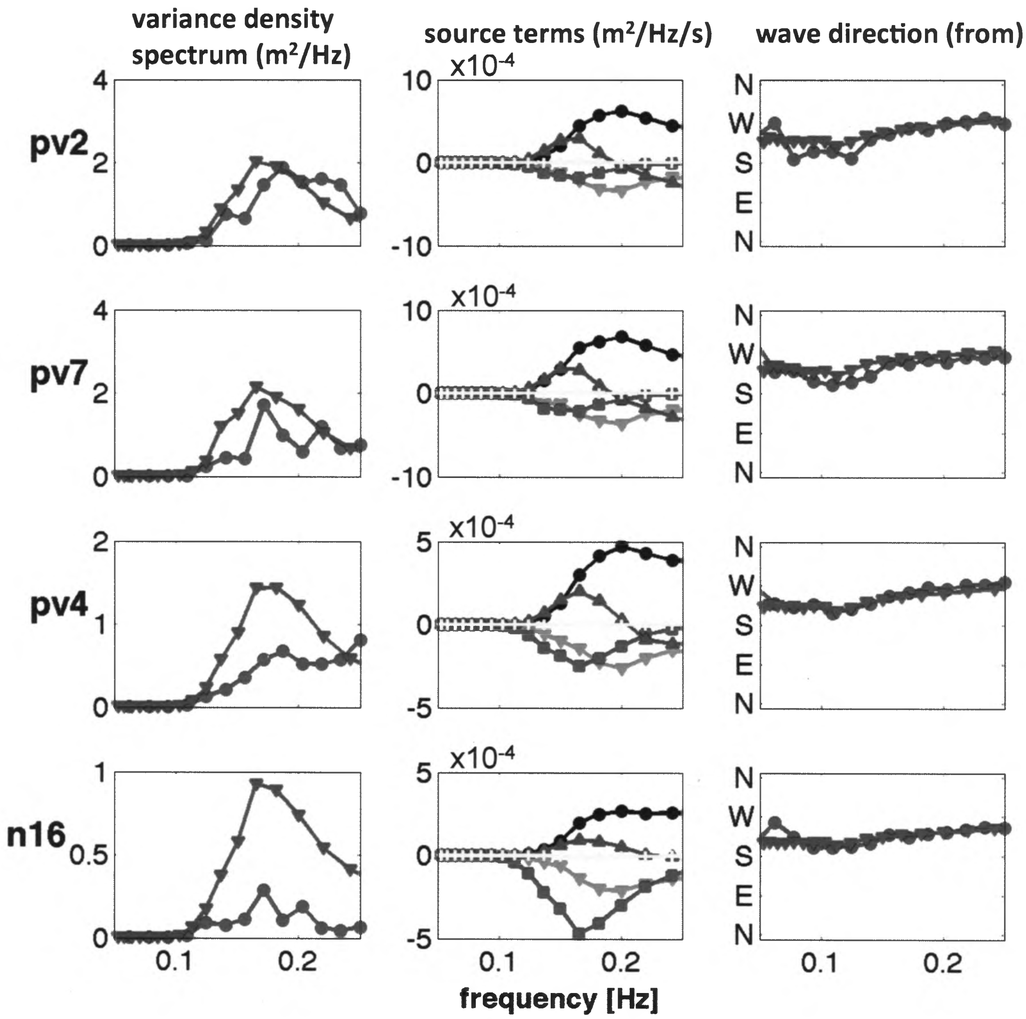

Figure 23. Left column shows the variance density spectrum for observations (red) and model (blue). Middle column shows SWAN source Right columns shows wave directions for observations (red) and model (blue).
Shown is March 7th for sensors pv2, pv7, pv4, n16, top to bottom.

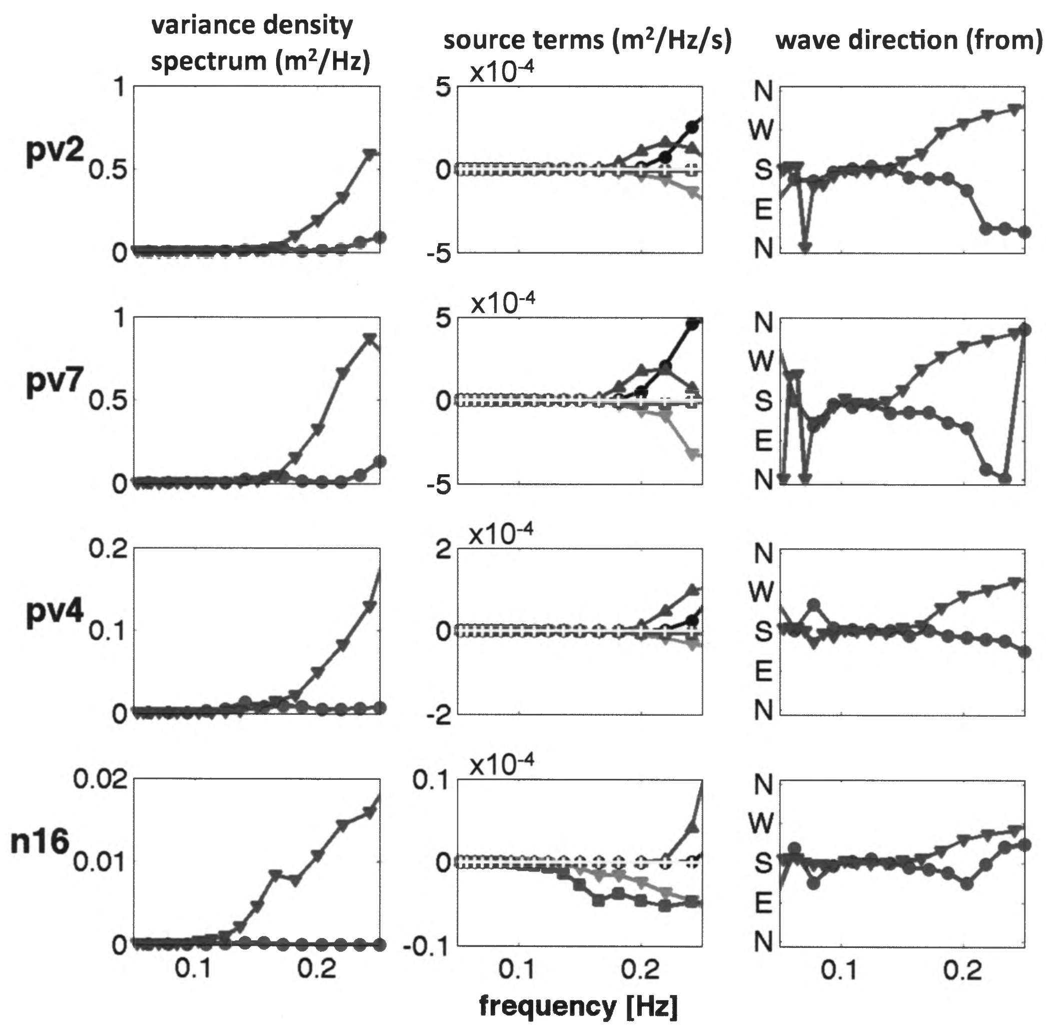

Figure 24 Left column shows the variance density spectrum for observations (red) and model (blue). Middle column shows SWAN source Right columns shows wave directions for observations (red) and model (blue).
Shown is March 24th for sensors pv2, pv7, pv4, n16, top to bottom.

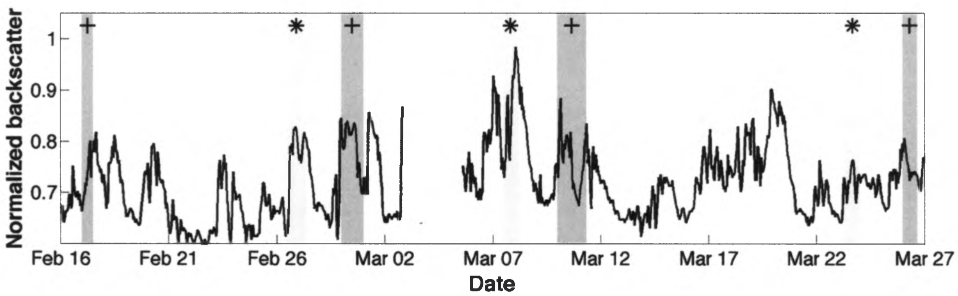

Figure 25. The normalized backscatter is shown at 1 m above the bottom (upper green curve shows pv9, upper black curve shows pv4), and at 5 m above the bottom (green curve shows again pv9 while black curve shows pv4). Crosses mark PD events, asterisks mark SG events.

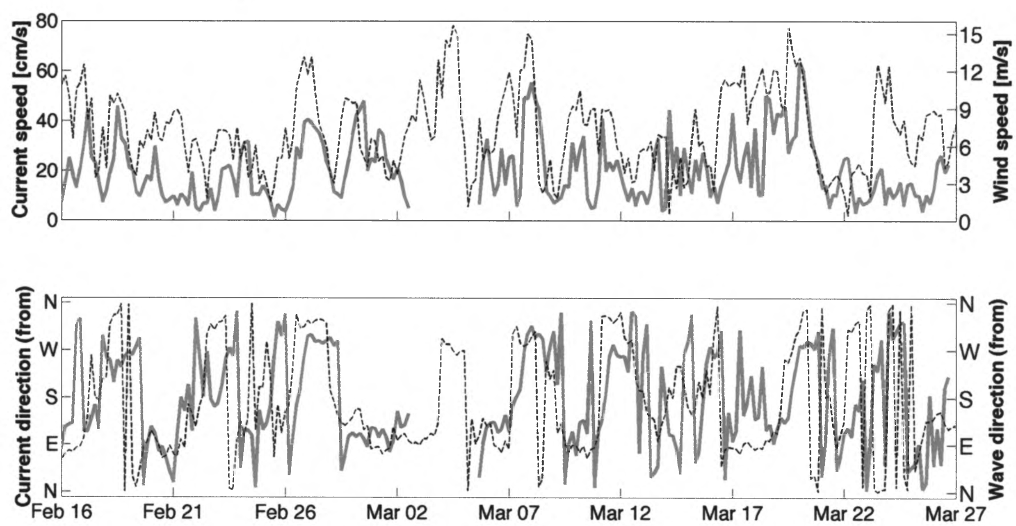

Figure 26. Shown are current speed (upper panel) and direction (lower panel) at station pv2. The black dashed lines shows wind speed and direction.

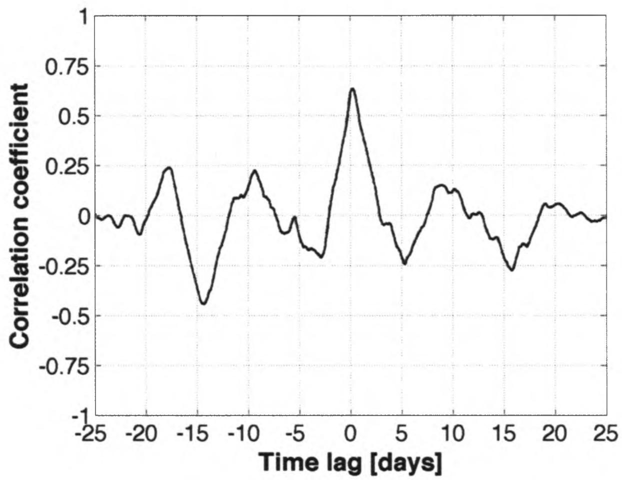

Figure 27. Shown is the correlation between current speed and backscatter intensity over the time lag.

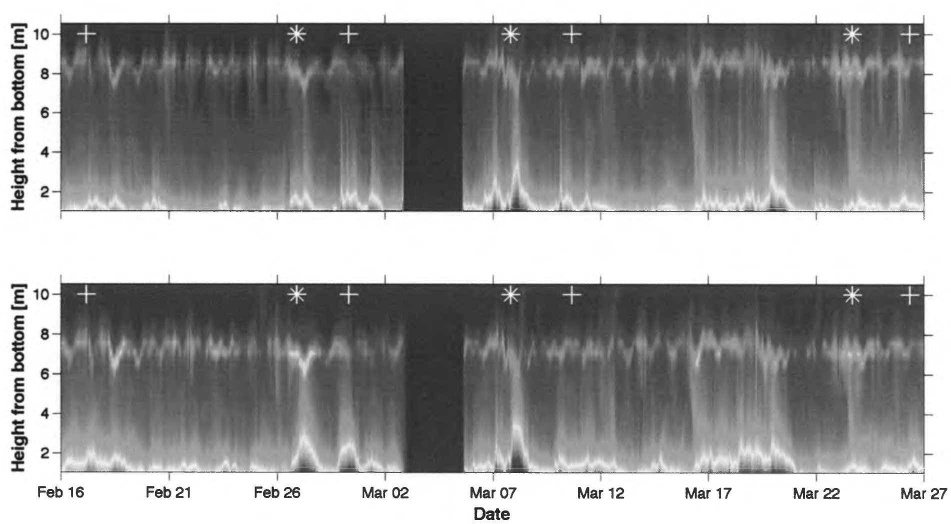

Figure 28. Backscatter intensity from ADCP from pv4 (upper panel) and pv9 (lower panel), arbitrary units. Red colors indicate high concentrations, while blue indicates no concentrations. Crosses mark PD events, asterisks mark SG events.

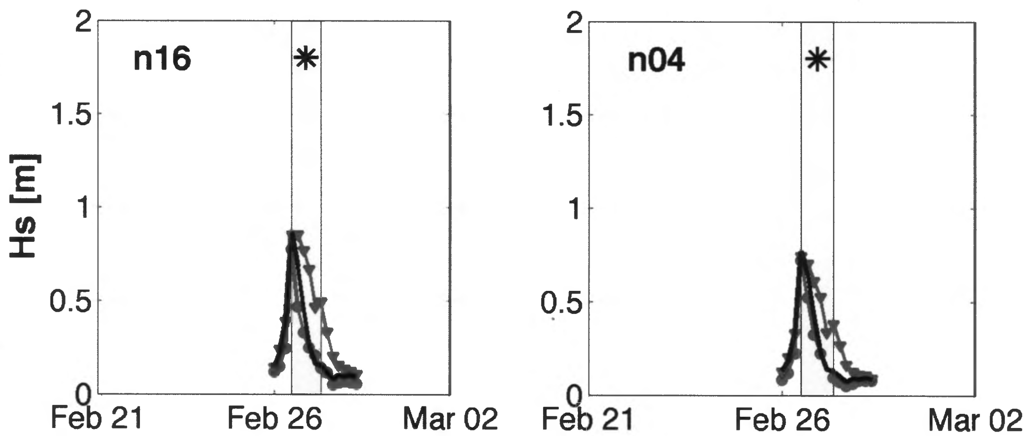

Figure 29. Shown is a comparison of observations (red curve), a model run with winds (blue curve), and a model run without winds (black curve).